

The uppermost mantle seismic velocity structure of West Antarctica from Rayleigh wave tomography: insights into tectonic structure and geothermal heat flow

J. P. O'Donnell<sup>1</sup>, G. W. Stuart<sup>1</sup>, A. M. Brisbourne<sup>2</sup>, K. Selway<sup>3</sup>, Y. Yang<sup>3</sup>, G. A. Nield<sup>4</sup>, P. L. Whitehouse<sup>4</sup>, A. A. Nyblade<sup>5</sup>, D. A. Wiens<sup>6</sup>, R. C. Aster<sup>7</sup>, S. Anandakrishnan<sup>5</sup>, A. D. Huerta<sup>8</sup>, T. Wilson<sup>9</sup> and J. P. Winberry<sup>8</sup>

(July 15, 2019)

(1) School of Earth and Environment, The University of Leeds, Leeds, LS2 9JT, UK

(2) British Antarctic Survey, Natural Environment Research Council, Cambridge CB3 0ET, UK

(3) Department of Earth and Planetary Science, Macquarie University, North Ryde, NSW 2109, Australia

(4) Department of Geography, Durham University, South Road, Durham, DH1 3LE, UK

(5) Department of Geosciences, The Pennsylvania State University, University Park, PA 16802, USA

(6) Department of Earth and Planetary Sciences, Washington University, St. Louis, MO 63160, USA

(7) Department of Geosciences, Colorado State University, Fort Collins, CO 80523, USA

(8) Department of Geological Sciences, Central Washington University, Ellensburg, WA 98926, USA

(9) School of Earth Sciences, Ohio State University, Columbus, OH 43210, USA

\* Corresponding author, [j.p.odonnell@leeds.ac.uk](mailto:j.p.odonnell@leeds.ac.uk)

# 1 Abstract

2 **Key words:** Antarctica, seismology, tectonics, lithosphere, mantle, heat flow

3 We present a shear wave model of the West Antarctic upper mantle to  $\sim 200$  km depth  
4 with enhanced regional resolution from the 2016-2018 UK Antarctic Seismic Network.

5 The model is constructed from the combination of fundamental mode Rayleigh wave  
6 phase velocities extracted from ambient noise (periods 8-25 s) and earthquake data  
7 by two-plane wave analysis (periods 20-143 s). We seek to (i) image and interpret

8 structures against the tectonic evolution of West Antarctica, and (ii) extract infor-  
9 mation from the seismic model that can serve as boundary conditions in ice sheet  
10 and glacial isostatic adjustment modelling efforts. The distribution of low veloc-

11 ity anomalies in the uppermost mantle suggests that recent tectonism in the West  
12 Antarctic Rift System (WARS) is mainly concentrated beneath the rift margins and  
13 largely confined to the uppermost mantle ( $< 180$  km). On the northern margin of

14 the WARS, a pronounced low velocity anomaly extends eastward from beneath the  
15 Marie Byrd Land dome toward Pine Island Bay, underlying Thwaites Glacier, but not  
16 Pine Island Glacier. If of plume-related thermal origin, the velocity contrast of  $\sim 5\%$

17 between this anomaly and the inner WARS translates to a temperature difference  
18 of  $\sim 125$ - $200^\circ\text{C}$ . However, the strike of the anomaly parallels the paleo-Pacific con-  
19 vergent margin of Gondwana, so it may reflect subduction-related melt and volatiles

20 rather than anomalously elevated temperatures, or a combination thereof. Motivated  
21 by xenolith analyses, we speculate that high velocity zones imaged south of the Marie  
22 Byrd Land dome and in the eastern Ross Sea Embayment might reflect the composi-

23 tional signature of ancient continental fragments. A pronounced low velocity anomaly  
24 underlying the southern Transantarctic Mountains (TAM) is consistent with a pub-  
25 lished lithospheric foundering hypothesis. Taken together with a magnetotelluric

26 study advocating flexural support of the central TAM by thick, stable lithosphere,

27 this points to along-strike variation in the tectonic history of the TAM. A high veloc-  
28 ity anomaly located in the southern Weddell Sea Rift System might reflect depleted  
29 mantle lithosphere following the extraction of voluminous melt related to Gondwana  
30 fragmentation. Lithospheric thickness estimates extracted from 1D shear wave veloc-  
31 ity profiles representative of tectonic domains in West Antarctica indicate an average  
32 lithospheric thickness of  $\sim 85$  km for the WARS, Marie Byrd Land, and Thurston Is-  
33 land block. This increases to  $\sim 96$  km in the Ellsworth Mountains. A surface heat flow  
34 of  $\sim 60$  mW/m<sup>2</sup> and attendant geotherm best explains lithospheric mantle shear wave  
35 velocities in the central WARS and in the Thurston Island block adjacent to Pine  
36 Island Glacier; a  $\sim 50$  mW/m<sup>2</sup> geotherm best explains the velocities in the Ellsworth  
37 Mountains, and a  $\sim 60$  mW/m<sup>2</sup> geotherm best explains a less well-constrained velocity  
38 profile on the southern Antarctic Peninsula. We emphasise that these are regional  
39 average (many hundreds of km) heat flow estimates constrained by seismic data with  
40 limited sensitivity to upper crustal composition.

# 1 Introduction

West Antarctica owes much of its tectonic heritage to the Jurassic breakup of Gondwana and ensuing dispersal of microplate fragments (e.g., Dalziel & Elliot, 1982; Dalziel, 1992). The development of the West Antarctic Rift System (WARS), the uplift of the Transantarctic Mountains (TAM) and the impact of a putative mantle plume beneath Marie Byrd Land (MBL) have dominated the late Cretaceous to Paleogene evolution of West Antarctica (Figure 1) (e.g., LeMasurier & Landis, 1996; Fitzgerald, 2002). With geological exposures limited by the West Antarctic Ice Sheet (WAIS), delineation of tectonic domains and recent tectonism is reliant on geophysical probing. Owing to the deployment of broadband seismometer arrays, the seismic structure of much of the Antarctic crust and upper mantle is now reasonably well mapped (e.g., An et al., 2015b; Heeszel et al., 2016; Shen et al., 2018).

We construct a shear wave model based on fundamental mode Rayleigh wave phase velocities focussing on the uppermost mantle structure (<200 km) of West Antarctica. The model offers enhanced regional resolution through the inclusion of stations from the 2016-2018 UK Antarctic Seismic Network (UKANET, Figure 1). In the first half of this paper we describe the seismic data, processing and inversion, and interpret the structures imaged against the tectonic evolution of West Antarctica. In the second half we extract information that can be used to improve the accuracy of ice sheet and glacial isostatic adjustment (GIA) modelling efforts. Geothermal heat flow moderates ice sheet behaviour: it affects the viscosity of basal ice and, if sufficiently high, can generate lubricating meltwater that reduces friction with the bed (e.g., Martos et al., 2017). Pine Island Glacier and Thwaites Glacier in West Antarctica (Figure 1) are of particular concern because they are thought susceptible to marine ice sheet instability (e.g., Barletta et al., 2018). GIA is sensitive to lithospheric thickness and its lateral variation (e.g., Nield et al., 2018). From our shear wave model, we extract lithospheric

67 thicknesses and model the regional average geotherms and heat flows best describing  
68 1D velocity profiles at representative tectonic locations in West Antarctica.

## 69 **2 Tectonic Setting**

70 East Antarctica was amalgamated from Archean nuclei in the Mesoproterozoic, even-  
71 tually forming the core of Gondwana (e.g., Dalziel, 1992). The Mesozoic fragmenta-  
72 tion of Gondwana was preceded by the emplacement of the Karoo-Ferrar large igneous  
73 province in East Antarctica and southern Africa at  $\sim 185$ -177 Ma (e.g., Storey & Kyle,  
74 1997; Fitzgerald, 2002, and references therein) and the development of the Weddell  
75 Sea Rift System (WSRS), a broad extensional/transensional province within a dis-  
76 tributed plate boundary between East and West Antarctica (e.g., Jordan et al., 2017).  
77 Karoo-Ferrar magmatism has been linked with a putative mantle plume in the proto-  
78 Weddell Sea region, potentially a driver for Gondwana breakup (e.g., Storey & Kyle,  
79 1997).

80 West Antarctica is regarded as an assemblage of discrete crustal blocks separated  
81 by subglacial depressions. Three of the main four blocks - the Antarctic Peninsula,  
82 Thurston Island and Marie Byrd Land - are fore-arc and magmatic-arc terranes de-  
83 veloped along the paleo-Pacific margin of Gondwana (e.g., Dalziel, 1992). The fourth  
84 block, the Haag-Ellsworth Whitmore (HEW) block, is regarded as an allochthonous  
85 continental fragment translated and rotated to its present location from an original  
86 pre-Gondwana-breakup position close to the East Antarctic plate and/or southern  
87 Africa. Exposed lithologies in the HEW block include a  $\sim 13$  km thick Paleozoic sedi-  
88 mentary sequence in the Ellsworth Whitmore Mountains, and Precambrian basement  
89 dated to  $\sim 1$  Ga in the Haag Nunataks (e.g., Storey & Kyle, 1997; Jordan et al., 2017,  
90 and references therein).

91 The tectonic regime in West Antarctica switched from compressional to extensional

92 following subduction of the Pacific-Phoenix spreading center at  $\sim 110$ -105 Ma. The  
93 West Antarctic Rift System formed as MBL and Thurston Island moved away from the  
94 East Antarctica craton, with the major WARS extensional phase occurring between  
95  $\sim 105$ -85 Ma (e.g., Fitzgerald, 2002, and references therein). Paleogene extension was  
96 limited to the western Ross Sea and accompanied by rapid exhumation and uplift of  
97 the Transantarctic Mountains. In MBL an estimated maximum  $\sim 3$  km of tectonic  
98 uplift associated with alkaline volcanism beginning at ca. 28-30 Ma is cited as evidence  
99 of a mantle plume (e.g., LeMasurier & Landis, 1996). Others favour a model of  
100 subduction-related alkaline magma genesis in MBL (e.g., Finn et al., 2005). Inferred  
101 Neogene reactivation of subglacial troughs in central West Antarctica has been linked  
102 with Neogene extensional pulses in the western Ross Sea (e.g., Lloyd et al., 2015, and  
103 references therein).

### 104 **3 Seismic Arrays**

105 The International Polar Year 2007-2008 motivated the first deployment of year-  
106 round broadband seismometer arrays in the interior of Antarctica. As part of the  
107 POLENET-ANET project, a backbone array was deployed across Antarctica (Figure  
108 1). The extant array comprises a mixture of cold-rated Gralp CMG-3T 120 s and  
109 Nanometrics Trillium 240 s seismometers sampling at 1 and 40 samples per second  
110 (sps).

111 Denser temporary arrays have intermittently supplemented the POLENET-ANET  
112 backbone array in West Antarctica, the most recent of which was the 2016-2018  
113 UKANET array. This consisted of 10 cold-rated Gralp CMG-3T 120 s seismometers  
114 sampling at 1 and 100 sps (Figure 1 and Table S1). The 2015-2017 POLENET-ANET  
115 mini-array was complementary in design and location to the UKANET array.

116 Additional coverage is provided by the Antarctic Seismographic Argentinean Ital-

117 ian Network (ASAIN), station PMSA of the Global Seismographic Network (GSN)  
118 and the 1997-1999 Seismic Experiment in Patagonia and Antarctica network (SEPA)  
119 shown in Figure 1.

## 120 4 Two-Plane-Wave Tomography

121 Surface wave amplitudes and phases observed across seismic arrays often exhibit ef-  
122 fects reminiscent of interference. This motivated Forysth & Li (2005) to model the  
123 wavefield as the superposition of two interfering plane waves. We applied this two-  
124 plane-wave method to fundamental mode Rayleigh waves recorded on the UKANET,  
125 POLENET-ANET, ASAIN and SEPA arrays and PMSA station over the periods  
126 1997-1999 and 2010-2018. To garner good quality waveforms, we examined earth-  
127 quakes with magnitudes  $\geq 5.5$  located within a distance of  $120^\circ$  of the composite  
128 seismic array. Earthquakes located within  $\sim 30^\circ$  of the array were excluded because  
129 the wave fronts cannot be considered planar at incidence.

130 An initial cull of earthquakes giving poor signal-to-noise ratio seismograms was carried  
131 out by visual inspection. Instrument responses were deconvolved from the remaining  
132 seismograms and these filtered into  $12 \times 10$  mHz wide frequency bands with centre  
133 periods ranging from 20 to 143 s using a zero-phase-shift, four-pole Butterworth filter  
134 centred at the period of interest (Figure 2). Next, for each earthquake a window was  
135 manually defined at each period to isolate the fundamental mode Rayleigh waves from  
136 other seismic phases and/or interfering lateral refractions. At each period, only those  
137 earthquakes yielding high signal-to-noise ratio Rayleigh waves at at least five stations  
138 were considered for two-plane-wave tomography (2PWT). Out of a total of  $\sim 2700$   
139 earthquakes screened, 457 were deemed suitable for analysis (Figure 2). Following  
140 Forysth & Li (2005), we assigned a prior data uncertainty of 10% to the phase and  
141 amplitude of each Rayleigh wave.



142 In the 2PWT inversion, at each period the Rayleigh wave phase velocity map best  
143 explaining phase and amplitude variations between stations was inferred on a grid  
144 with a node spacing of 100 km spanning West Antarctica. Being predicated on the  
145 assumption of planar wave fronts, the validity of 2PWT varies inversely with the areal  
146 extent of the seismic array. In response, we subdivided the expansive composite array  
147 into three sub-arrays approximately coincident with the Antarctic Peninsula, eastern  
148 West Antarctica and central West Antarctica. In this scheme, a given earthquake  
149 is effectively treated as three separate earthquakes, each incident on one of the sub-  
150 arrays. Following Yang & Forsyth (2006), finite frequency sensitivity kernels were  
151 used to represent the sensitivities of Rayleigh wave phases and amplitudes to struc-  
152 ture. A smoothing length scale of 140 km gave the best compromise between unduly  
153 rough models arising from over-fitting data at the shortest length scales and under-fit  
154 models at the longest length scales (Figure S1). Using the 1D average phase velocity  
155 curve inferred by Heeszel et al. (2016) as a starting model, we initially inverted for  
156 a 1D average phase velocity curve representing our study area to serve as a starting  
157 model for the 2D tomographic inversions (Figure 3).

## 158 **5 Rayleigh Wave Phase Velocities**

159 Figure 4 shows the inferred 2D Rayleigh wave phase velocity uncertainty, calculated  
160 from the posterior model covariance matrix, at periods 25, 80 and 125 s. As expected,  
161 the uncertainty is least where the concentration of seismic stations is greatest and  
162 increases toward the grid periphery. Superimposed on the lateral variations is a  
163 trend of increasing uncertainty with increasing period, a reflection of the progressively  
164 increasing wavelength of the Rayleigh waves and hence decreasing resolution.

165 Figure 4 also shows the resolving capability of the inversion. The resolution matrix  
166 indicates that the morphology of velocity anomalies of length scale 400 km is recovered

167 with high fidelity within the polygon on Figure 4 at all periods. At periods 125 and  
168 143s there is some diminution in amplitudes at this length scale, but at all shorter  
169 periods amplitude recovery is generally better than 90%. Amplitude resolution at  
170 periods 125 and 143s reaches this level for a length scale of 500 km.

171 The resolution matrix gives an overly optimistic picture of resolution at peripheral  
172 grid regions beyond the footprint of the seismic array. In subsequent plots we confine  
173 our discussion to the region enclosed by the polygon. Within this region (i) phase  
174 velocity uncertainty is generally less than  $\sim 0.02-0.03$  km/s at periods below 80 s and  
175 less than  $\sim 0.05$  km/s at periods 100-143 s, (ii) the resolution matrix indicates that  
176 velocity structure of length scale 400-500 km is imaged with high fidelity and (iii)  
177 imaged velocity structure transitions credibly between periods.

178 Figure 5 shows Rayleigh wave phase velocity maps at selected periods. At periods  
179  $\sim 20-30$  s Rayleigh wave propagation is most sensitive to variations in crustal thick-  
180 ness: if the crust is thick, Rayleigh waves at these periods largely sample lower crustal  
181 rock, whereas if the crust is thin they largely sample seismically-faster mantle rock.  
182 At 25 s for example, relatively slower phase velocities coincident with the TAM, the  
183 HEW block, MBL, the southern Antarctic Peninsula and northern WSRS are consis-  
184 tent with thicker crust (e.g., Chaput et al., 2014; O'Donnell & Nyblade, 2014; Shen  
185 et al., 2018). In contrast, relatively faster phase velocities underlying the Ross and  
186 Amundsen Sea Embayments in the WARS and in the southern WSRS are likely the  
187 signature of mantle rock, and hence thinner crust.

188 At periods 40 s and above the Rayleigh wave phase velocities predominantly reflect  
189 uppermost mantle structure. The geological dichotomy of Antarctica is here ap-  
190 parent: slower phase velocities characterising the West Antarctic uppermost mantle  
191 contrast with faster velocities underlying East Antarctica. Prominent slow phase ve-  
192 locity anomalies at these periods occur beneath MBL and a portion of the southern  
193 TAM. Notably, the slow velocity anomaly underlying MBL extends eastward beyond

194 the MBL topographic dome toward Pine Island Bay. Offshore MBL a slow velocity  
195 anomaly coincides with the location of the Marie Byrd Seamounts and is conceivably  
196 the source thereof.

## 197 **6 Shear Wave Velocities**

198 At each grid node, a phase velocity dispersion curve (periods 20-143 s) was extracted  
199 by sampling the 2PWT phase velocity maps. These curves were merged with counter-  
200 parts extracted from ambient noise tomography (ANT) Rayleigh wave phase velocity  
201 maps developed by the authors (O'Donnell et al., 2018). The shorter period ANT  
202 data (periods 8-25 s) have a greater sensitivity to crustal structure than the 2PWT  
203 data. Figure 6 compares ANT- and 2PWT-inferred phase velocity maps at 25 s and  
204 shows an example of a composite 8-143 s phase velocity dispersion curve obtained by  
205 weighted least squares polynomial regression of the ANT- and 2PWT-curves. Dif-  
206 ferences in processing, inversion and regularisation schemes result in minor disparity  
207 between ANT- and 2PWT-inferred velocities, but they generally agree within uncer-  
208 tainty bounds at overlapping periods. The areal extent of the ANT model domain,  
209 however, is less extensive than the 2PWT domain, so merged ANT-2PWT dispersion  
210 curves are restricted to the ANT domain. The phase velocity dispersion curves were  
211 subsequently inverted for 1D shear wave velocity structure. Because Rayleigh waves  
212 are most sensitive to vertically-polarised shear wave velocity,  $V_{SV}$ , we inferred  $V_{SV}$   
213 rather than isotropic  $V_S$ .

214 The  $V_{SV}$  models were parameterised by ice and/or water layers overlying crustal  
215 and uppermost mantle layers. Ice thicknesses and water depths were taken from  
216 BEDMAP2 and allowed to vary within their uncertainty limits (Fretwell et al., 2013).  
217 The ice shear wave velocity was permitted to range between 1.82-2.02 km/s with a  
218 density fixed at 910 kg/m<sup>3</sup>. We opted to not invert for a sedimentary layer because (1)

219 Rayleigh waves have limited sensitivity to shallow crustal structure in the period range  
220 considered and (2) sediment thickness estimates to guide the inversion are extremely  
221 limited. The 1D  $V_{SV}$  structure of the underlying crustal layer was parameterised  
222 using 4 cubic B-splines and a crustal thickness permitted to vary  $\pm 5$  km from initial  
223 estimates extracted from the An et al. (2015b) Antarctic crustal model. The 1D  
224 uppermost mantle  $V_{SV}$  structure was parameterised using 5 cubic B-splines to a depth  
225 of 250 km, below which PREM  $V_{SV}$  values were adopted. In a Bayesian framework,  
226 we permitted crustal and uppermost mantle  $V_{SV}$  velocities to explore a broad  $\pm 20\%$   
227 range around initial PREM  $V_{SV}$  velocities, a range which encompasses published  
228 Antarctic velocity models (e.g., An et al., 2015b). This suite of constraints informed  
229 the prior model probability density function (PDF).

230 The likelihood function for dispersion curve prediction used the *Mineos* package  
231 (<https://geodynamics.org/cig/software/mineos/>). Crustal compressional wave  
232 velocities and densities were scaled from inferred shear wave velocities using regres-  
233 sions reported in Brocher (2005), while upper mantle counterparts were scaled using  
234 a  $V_p/V_s$  ratio of 1.74 and Birch’s law (Birch, 1961). PREM Q values were used  
235 to correct for anelastic attenuation. A Markov chain Monte Carlo sampling scheme  
236 based on the Delayed Rejection Adaptive Metropolis algorithm built the posterior  
237 model PDF from the final 2,500 accepted models of 100,000 simulations (Guo et al.,  
238 2016, and references therein).

## 239 **6.1 Tectonic Interpretation**

240 Figure 7 shows a selection of 1D  $V_{SV}$  profiles representative of their parent tectonic  
241 domains in West Antarctica: station PIG3 lies adjacent to Pine Island Glacier in the  
242 Thurston Island block; station FOWL is close to the Haag Nunataks of the HEW  
243 block; node 1624 is in the Ellsworth Mountains of the HEW block; station BREN

244 is at Brenneke Nunatak on the southern Antarctic Peninsula; station SILY is at  
245 Mount Sidley in MBL; station BYRD is in the central WARS; station DUFK is at  
246 the Dufek Intrusion at the margin of the WSRS; and station SURP is at the southern  
247 TAM front (see Figure 1 and Table S1). The average standard deviation of inferred  
248 mantle  $V_{SV}$  velocities is generally less than  $\sim 0.075$  km/s, increasing to  $\sim 0.1$  km/s  
249 for locations (e.g., BREN) at the periphery of the modelled domain. The average  
250 standard deviation of inferred crustal velocities is generally less than  $\sim 0.1$  km/s.

251 The crust thickens from  $\sim 25$  km in the Thurston Island block (PIG3), to  $\sim 29$  km at  
252 the Haag Nunataks (FOWL), to  $\sim 37$  km in the Ellsworth Mountains (node 1624). In  
253 the southern Antarctic Peninsula (BREN) the crust is  $\sim 39$  km; however, this profile  
254 is the least well constrained of those displayed due to the peripheral location (see  
255 Figures 1 and 5). The crust is  $\sim 27$  km thick in MBL (SILY),  $\sim 26$  km in the central  
256 WARS (BYRD), and  $\sim 36$  km thick at the Dufek Intrusion (DUFK). The signature  
257 of a sharp crust-mantle transition is absent at the southern TAM front (SURP), so  
258 the estimated crustal thickness of  $\sim 26$  km is less well constrained than the other  
259 locations. These estimates of crustal thickness are consistent with preceding studies  
260 (e.g., Chaput et al., 2014; Ramirez et al., 2017; O'Donnell et al., 2017).

261 All  $V_{SV}$  depth profiles show a high-velocity seismic mantle “lid”. Defining the seismic  
262 lithosphere-asthenosphere boundary (LAB) at the strongest negative velocity gradient  
263 at the base of the high-velocity lid (e.g., Eaton et al., 2009), the seismic LAB is at  
264  $\sim 85$  km depth beneath the Thurston Island block (PIG3), MBL (SILY), the central  
265 WARS (BYRD) and southern TAM front (SURP). The seismic LAB depth increases  
266 to  $\sim 92$  km at the Dufek Intrusion (DUFK) and  $\sim 96$  km at the Ellsworth Mountains  
267 (node 1624) (Figure 7). Alternative definitions of the seismic LAB exist (e.g., Eaton  
268 et al., 2009); for example, adopting the onset of the negative velocity gradient at the  
269 lid base would reduce our seismic LAB depth estimates by  $\sim 10$ - $20$  km. The lid at  
270 the southern TAM front (SURP), and at MBL (SILY) to a lesser extent, is underlain

271 by a pronounced low velocity zone: at  $\sim 130$  km depth,  $V_{SV}$  is  $\sim 4.05$ - $4.15$  km/s at  
272 SURP and  $\sim 4.15$ - $4.20$  km/s at SILY. In contrast to SURP and SILY, at BYRD in  
273 the central WARS  $V_{SV}$  is  $\sim 4.20$ - $4.30$  km/s at 130 km depth.

274 2D  $V_{SV}$  maps were constructed by gridding the suite of 1D  $V_{SV}$  profiles (Figures  
275 8 and 9). At 25 km depth, velocities strongly characteristic of crustal lithologies  
276 ( $V_{SV} < \sim 4.0$  km/s) are evident beneath the southern TAM, the WSRS, the HEW  
277 block and the Antarctic Peninsula. The slowest velocities at this depth are located  
278 beneath the southern TAM and Ellsworth Mountains. However, the ANT resolu-  
279 tion degrades on the Peninsula (O'Donnell et al., 2018), so the inferred crustal  $V_{SV}$   
280 velocities there are likely overestimated; gravity data suggest that crustal thickness  
281 on the southern Peninsula is comparable to that beneath the Ellsworth Mountains  
282 (e.g., O'Donnell & Nyblade, 2014). Faster velocities - indicative of thinner crust  
283 - characterise the WARS at this depth, with velocities indicative of mantle rock  
284 ( $V_{SV} > \sim 4.3$  km/s) apparent in the Ross and Amundsen Sea Embayments. Crust  
285 thinner than 25 km at these locations is consistent with preceding studies (e.g., Cha-  
286 put et al., 2014; Shen et al., 2018). Our model suggests that thicker crust in the WARS  
287 is found in a region extending south from the MBL topographic dome, consistent with  
288 Chaput et al. (2014).

289 The outstanding feature at 60 km depth is the high velocity anomaly located between  
290 the Ellsworth Mountains and the Dufek Intrusion/Pensacola Mountains, also seen  
291 in cross-section AA' in Figure 9. Storey & Kyle (1997) posit that plume-generated  
292 Ferrar magmas could have ponded in large magma chambers, like that from which  
293 the Dufek Intrusion crystallized (see Figure 1 for location), and from these spread  
294 along the length of the TAM, explaining the chemical uniformity of Ferrar exposures  
295 over large distances. Shear velocities of the magnitude we infer ( $\sim 4.6$ - $4.8$  km/s) in the  
296 lithospheric mantle beneath the southern WSRS are characteristic of depleted, cra-  
297 tonic lithosphere. We speculate that the high velocity anomaly might reflect depleted

298 mantle lithosphere following the extraction of voluminous melt related to Gondwana  
299 breakup.

300 The absence of a sharp velocity contrast at the eastern margin of the WSRS is con-  
301 sistent with the WSRS being a broad extensional/transensional province within a  
302 distributed plate boundary between East and West Antarctica (Jordan et al., 2017).  
303 The conventional interpretation of the TAM as the margin of East Antarctica in the  
304 Weddell Sea Embayment may need to be re-visited.

305 The seismic signature of the cratonic margin of East Antarctic is clear along the south-  
306 ern and northern TAM front at depth slices 120 and 150 km. However, the boundary  
307 is located behind the southern TAM front. Depth slices at 90, 120 and 150 km reveal  
308 a pronounced low velocity anomaly underlying the southern TAM front (minimum  
309  $V_{SV}$  is  $\sim 4.05$  km/s). Shen et al. (2017, 2018) also image this low velocity anomaly  
310 and attribute it to lithospheric foundering, a mechanism they invoke to explain the  
311 uplift of the TAM. The southern portions of our cross-sections CC' and DD' in Fig-  
312 ure 9 does not contradict their interpretation. Taken together with a magnetotelluric  
313 study advocating flexural support of the central TAM by thick, high electrical resis-  
314 tivity lithosphere (Wannamaker et al., 2017), and seismic studies advocating flexural  
315 support of the northern TAM by warm, buoyant upper mantle impinging from the  
316 adjacent WARS (e.g., Lawrence et al., 2006), this points to along-strike variation in  
317 the tectonic history of the TAM.

318 We do not interpret structure below 200 km depth, but seismic velocities character-  
319 istic of cratonic lithosphere are inferred to persist to depths of  $\sim 220$ -250 km beneath  
320 East Antarctica (e.g., Ritzwoller et al., 2001; Shen et al., 2018). The thickness of the  
321 seismic lid beneath the Ellsworth Mountains ( $\sim 95$ -100 km) is substantially less than  
322 that underlying the East Antarctic craton (see cross-section AA in Figure 9). This  
323 points to modification of the Precambrian lithosphere beneath the Ellsworth Whit-  
324 more Mountains, which Lloyd et al. (2015) suggest reflects lithospheric foundering

325 related to Gondwana breakup, magmatic intrusion, and subsequent development of  
326 the WARS.

327 At 90 km depth, high velocity zones ( $V_{SV} \sim 4.5\text{-}4.55$  km/s) are apparent south of the  
328 MBL dome and in the eastern Ross Sea Embayment. White-Gaynor et al. (2019)  
329 propose that relatively faster upper mantle  $V_P$  velocities imaged beneath the eastern  
330 Ross Sea Embayment by body-wave tomography reflect lithosphere that may not  
331 have been reheated by the Cenozoic rifting that affected other parts of the WARS.  
332 Xenolith analyses suggest that lithospheric mantle beneath MBL and circum-Pacific  
333 Phanerozoic continental crustal terranes in south east Australia and other locations in  
334 Zealandia preserves ancient Archean-Proterozoic peridotite components (e.g., Handler  
335 et al., 2003; Liu et al., 2015, and references therein). Handler et al. (2003) suggest  
336 that the Proterozoic mantle beneath MBL might have a provenance in the East  
337 Antarctic craton, while Liu et al. (2015) invoke a model whereby ancient depleted  
338 mantle domains are dispersed in the convecting mantle and reappear beneath young  
339 continents. As a possible alternative to the White-Gaynor et al. (2019) model, we  
340 suggest that the high velocity zones imaged south of the MBL dome and in the eastern  
341 Ross Sea Embayment might reflect the compositional signature of ancient continental  
342 fragments.

343 Cenozoic alkaline volcanism in MBL, which started at  $\sim 28\text{-}30$  Ma, was preceded by  
344 uplift of the peneplained surface of the MBL block. This, and the isotopic signa-  
345 ture of a high-U/Pb (HIMU) mantle reservoir in the rocks, suggests plume-related  
346 volcanism (e.g., LeMasurier & Landis, 1996, and references therein). Anomalously  
347 low seismic velocity upper mantle beneath the MBL dome is consistently imaged,  
348 but the unambiguous signature of a plume “tail” extending deeper into the mantle  
349 has thus far evaded detection (e.g., Lloyd et al., 2015; Shen et al., 2018). At the  
350 northern margin of the WARS, we image a pronounced low velocity anomaly stretch-  
351 ing eastward from beneath the MBL dome to Pine Island Bay, underlying Thwaites



352 Glacier, but not Pine Island Glacier. The velocity contrast between this perturbed  
353 upper mantle and that of the inner WARS ( $\sim 5\%$ ) is consistent with estimates from  
354 Lloyd et al. (2015) and Shen et al. (2018). Assuming temperature is the dominant  
355 control on lateral variations in seismic velocity in the upper mantle, this contrast  
356 translates to a thermal anomaly of  $\sim 125\text{-}200^\circ\text{C}$  (e.g., Faul & Jackson, 2005). Finn  
357 et al. (2005) favour a model of subduction-related alkaline magma genesis in MBL.  
358 They suggest that protracted Paleozoic-Mesozoic subduction along the Paleo-Pacific  
359 margin of Gondwana resulted in metasomatic enrichment of the upper mantle; detach-  
360 ment of subducted slabs in the late Cretaceous along the former Gondwana margin  
361 induced Rayleigh-Taylor instabilities, triggering lateral and vertical flow of warm Pa-  
362 cific mantle. They suggest that this catalysed melting of the metasomatised upper  
363 mantle, resulting in Cenozoic alkaline magmatism. Emry et al. (2014) also suggest  
364 that subduction-related volatiles might explain negative peaks in receiver functions  
365 above the mantle transition zone in West Antarctica. The velocity anomaly we image  
366 strikes approximately parallel to the convergent paleo-Pacific margin of Gondwana,  
367 so it conceivably encodes the signature of subduction-related melt and volatiles rather  
368 than, or in addition to, plume-related anomalously elevated temperatures. Additional  
369 data (e.g., compressional wave velocities, resistivity measurements) are needed to dif-  
370 ferentiate between chemical and thermal contributions to the observed low shear wave  
371 velocity anomaly, and hence between subduction and plume hypotheses. A less pro-  
372 nounced low velocity zone underlying the southern Antarctica Peninsula to  $\sim 100$  km  
373 depth may similarly encode the signature of Mesozoic subduction and/or a remnant  
374 thermal signature of the mid-Cretaceous Palmer Land orogeny affecting the southern  
375 Peninsula (e.g., Vaughan et al., 2002).

376 A low velocity anomaly underlying the Bentley Subglacial Trench in the central WARS  
377 is evident at depth slices 90, 120 and 150 km (minimum  $V_{SV}$  is  $\sim 4.15\text{-}4.20$  km/s).  
378 Lloyd et al. (2015) imaged the same velocity anomaly, arguing that it represents

379 a thermal anomaly associated with focussed Neogene extension. They suggest that  
380 surrounding faster velocities in the WARS may reflect Late Cretaceous/early Cenozoic  
381 extension whose thermal perturbation due to rifting has largely dissipated.

382 The  $V_{SV}$  maps suggests that - the Bentley Subglacial Trench aside - current tecton-  
383 ism in the WARS is concentrated beneath the rift margins. By 180 km depth, lateral  
384 variations in velocity across West Antarctica are much reduced, as is the contrast  
385 with East Antarctica. The reduced lateral velocity variations within West Antarc-  
386 tica suggest that rift-related tectonism is largely confined to the uppermost mantle  
387 (<180 km depth).

## 388 **6.2 Geotherms and Heat Flow**

389 Accurate estimation of geothermal heat flow in West Antarctica is pressing given the  
390 considered vulnerability of the WAIS to marine ice sheet instability (e.g., Barletta  
391 et al., 2018). We seek the steady-state conductive geotherms, and hence surface  
392 heat flows, best explaining inferred  $V_{SV}$  profiles at representative tectonic locations  
393 in West Antarctica. The selected stations/grid nodes have  $V_{SV}$  profiles typical of  
394 their parent tectonic domains: the southern Antarctic Peninsula (BREN), the central  
395 WARS (BYRD), the Thurston Island block (PIG3, located adjacent to Pine Island  
396 Glacier), and the Ellsworth Mountains of the HEW block (grid node 1624) (Figure  
397 7). Based on the location of low  $V_{SV}$  velocity anomalies in Figure 8, steady-state  
398 conduction is probably a reasonable assumption at these locations. Locations for  
399 which steady-state conduction is unlikely, for example, in MBL and the southern  
400 TAM, are beyond the scope of the present study. A companion study to define 3D  
401 variations in mantle viscosity beneath West Antarctica will use the  $V_{SV}$  model as a  
402 3D gauge of uppermost mantle temperatures.

403 We use the Abers & Hacker (2016) MATLAB toolbox to predict the elastic, isotropic

404  $V_S$  of average spinel peridotite and garnet peridotite compositions of lithospheric  
 405 mantle for candidate geotherms. The spinel peridotite composition represents aver-  
 406 age continental lithospheric mantle based on spinel lherzolite xenoliths (McDonough,  
 407 1990), and the garnet peridotite composition represents “tecton” (i.e., formed or mod-  
 408 ified at  $< 1$  Ga) lithospheric mantle based on garnet xenocrysts (Griffin et al., 2009).  
 409 For fertile peridotites, the transition from spinel peridotite to garnet peridotite occurs  
 410 at  $\sim 1.5$  GPa ( $\sim 45$ -50 km depth) (e.g., Lee, 2003, and references therein).

411 For a layer of thickness  $\Delta z$  with constant radiogenic heat production,  $A$ , and con-  
 412 stant thermal conductivity,  $k$ , undergoing 1D steady-state heat conduction, the tem-  
 413 perature and heat flow at the bottom of the layer ( $T_b$  and  $q_b$ , respectively) can be  
 414 determined from the temperature and heat flow at the top of the layer ( $T_t$  and  $q_t$ ,  
 415 respectively) using

$$T_b = T_t + \frac{q_t}{k}\Delta z - \frac{A}{2k}\Delta z^2 \quad (1)$$

416 and

$$q_b = q_t - A\Delta z \quad (2)$$

417 (e.g., Hasterok & Chapman, 2011; Furlong & Chapman, 2013). A 1D steady-state  
 418 conductive geotherm is obtained by applying these equations to successive layers  
 419 and iterating to account for the temperature and pressure dependence of thermal  
 420 conductivity.

421 Under steady-state conditions, surface heat flow represents the sum of heat flow into  
 422 the base of the lithosphere and the integrated radiogenic heat production within the  
 423 lithosphere. Direct measurement of radiogenic heat production indicates generally  
 424 high values in felsic rocks ( $\sim 2$ -3  $\mu\text{W}/\text{m}^3$ ), low values in mafic rocks ( $\sim 0.2$   $\mu\text{W}/\text{m}^3$ ),  
 425 and very low values in ultramafic rocks ( $\sim 0.02$   $\mu\text{W}/\text{m}^3$ ) (e.g., Furlong & Chapman,  
 426 2013). We segregate our 1D  $V_{SV}$  crustal profiles into upper (felsic) and lower (mafic)  
 427 portions based on the observed velocities, with each portion comprising a sequence

428 of 1 km thick layers (i.e.,  $\Delta z = 1$  km). A global compilation of seismic velocities  
 429 suggests that middle continental crust is dominated by  $V_P = 6.5$ - $6.8$  km/s and  $V_P/V_S$   
 430  $= 1.65$ - $1.80$  (Hacker et al., 2015), implying an upper-middle crust transition at  $V_S =$   
 431  $3.61$ - $3.78$  km/s. We adopt  $V_{SV} < 3.7$  km/s as indicative of upper crust and  $V_{SV} >$   
 432  $3.7$  km/s as indicative of combined middle and lower crust - hereafter referred to  
 433 as lower crust. To the lower crust we assign a heat production of  $0.4 \mu\text{W}/\text{m}^3$  (e.g.,  
 434 Hasterok & Chapman, 2011). We regard  $V_{SV} > 4.3$  km/s as defining the transition to  
 435 the lithospheric mantle, where we fix heat production at  $0.02 \mu\text{W}/\text{m}^3$  (e.g., Hasterok  
 436 & Chapman, 2011; Furlong & Chapman, 2013). Upper crustal heat production,  $A_{UC}$ ,  
 437 is assigned according to

$$A_{UC} = (1 - F)q_S/D, \quad (3)$$

438 where  $D$  is the thickness of the upper crust (defined by  $V_{SV} < 3.7$  km/s),  $q_S$  is surface  
 439 heat flow and  $F$  is a partition coefficient defining the ratio of “basal” heat flow (the  
 440 combination of middle/lower crustal heat production, lithospheric mantle heat pro-  
 441 duction, and sub-lithospheric heat flow) to surface heat flow (e.g., Hasterok & Chap-  
 442 man, 2011; Furlong & Chapman, 2013). With observed seismic velocities controlling  
 443 the definition of upper crustal, lower crustal and lithospheric mantle layers, the par-  
 444 tition model facilitates the convenient parameterisation of steady-state geotherms in  
 445 terms of a single variable: surface heat flow. Using a preferred partition coefficient  
 446 of  $F = 0.74$  (Hasterok & Chapman, 2011), we vary  $q_S$  in increments of  $5 \text{ mW}/\text{m}^2$  to  
 447 produce candidate steady-state conductive geotherms at locations representative of  
 448 the southern Antarctic Peninsula (BREN), the central WARS (BYRD), the Thurston  
 449 Island block in the vicinity of Pine Island Glacier (PIG3), and the Ellsworth Moun-  
 450 tains in the HEW block (grid node 1624). Crustal thermal conductivity is calculated  
 451 following Furlong & Chapman (2013) and lattice and radiative contributions to ther-  
 452 mal conductivity in the lithospheric mantle calculated following Hasterok & Chapman  
 453 (2011).

454 Attendant elastic, isotropic  $V_S$  velocities for the lithospheric mantle are calculated  
455 from the geotherms using Abers & Hacker (2016). To facilitate comparison with the  
456 observed anelastic,  $V_{SV}$  velocities, the calculated velocities are converted to anelastic,  
457  $V_{SV}$  velocities assuming PREM Q values and 4% radial anisotropy in the lithospheric  
458 mantle of West Antarctica (Ritzwoller et al., 2001). We do not attempt to model the  
459 crustal velocity profiles due to the more complex compositional heterogeneity.

460 Figure 10 shows geotherms best explaining the observed  $V_{SV}$  profiles for the Antarc-  
461 tic Peninsula (BREN), the central WARS (BYRD), the Ellsworth Mountains of the  
462 HEW block (node 1624), and the Thurston Island block in the vicinity of Pine Island  
463 Glacier (PIG3). We present geotherms corresponding to lower-bound, upper-bound  
464 and preferred heat flows.

465 For a tecton garnet peridotite composition, a surface heat flow of  $\sim 60$  mW/m<sup>2</sup> at  
466 BYRD and PIG3 and  $\sim 50$  mW/m<sup>2</sup> at node 1624 yield geotherms that explain the  
467 inferred  $V_{SV}$  of the lower lithospheric mantle reasonably well. We define the ther-  
468 mal LAB as the intersection of the conductive geotherm and a mantle adiabat based  
469 on a mantle potential temperature of 1300°C and adiabatic temperature gradient of  
470 0.45°C/km (e.g., Katsura et al., 2010). While the seismic and thermal LABs need  
471 not coincide (e.g., Eaton et al., 2009), they do covary and occur within  $\sim 5$ -15 km  
472 of each other at these locations for our preferred heat flows. The  $V_{SV}$  profile of the  
473 upper lithospheric mantle at these three locations is more problematic. At PIG3 and  
474 node 1624 in particular, the predicted upper lithospheric mantle  $V_{SV}$  is beyond one  
475 standard deviation of the observed mean  $V_{SV}$  for the garnet peridotite composition.  
476 The spinel peridotite composition reduces the predicted  $V_{SV}$  somewhat, but a dis-  
477 crepancy persists. Potential contributors to the discrepancy include (1) inadequate  
478 capture of the true velocity structure at the crust-mantle transition, (2) the adoption  
479 of constant radial anisotropy of strength 4% in the lithospheric mantle, (3) the use of  
480 PREM Q values to convert from elastic to anelastic velocities, (4) the assumed spinel

481 peridotite and garnet peridotite compositions, and (5) the partition model of heat  
482 production. Surface waves are less sensitive to sharp impedance contrasts than they  
483 are to average velocity structure. The addition of receiver function data would better  
484 constrain velocity structure at the crust-mantle transition (e.g., Shen et al., 2018)  
485 and mitigate (1). Within the remit of Antarctic seismology, the development of Love  
486 wave and attenuation tomography models would eliminate the need for assumptions  
487 (2) and (3), respectively.

488 Our preferred surface heat flow of  $\sim 60 \text{ mW/m}^2$  at BYRD is largely consistent with  
489 inferences based on satellite magnetic data ( $\sim 55\text{-}65 \text{ mW/m}^2$ ; Fox Maule et al., 2005)  
490 and seismic data ( $\sim 70 \text{ mW/m}^2$ ; An et al., 2015a)) at that location, and an inferred  
491 broad scale heat flow of  $60\text{-}70 \text{ mW/m}^2$  for east-central West Antarctica based on  
492 magnetotelluric data (Wannamaker et al., 2017). Our preferred surface heat flow  
493 of  $\sim 60 \text{ mW/m}^2$  is similarly broadly consistent with a heat flow of  $\sim 60\text{-}65 \text{ mW/m}^2$   
494 inferred by geodynamic modelling of WARS evolution (van Wijk et al., 2008) and  
495 a heat flow of  $70 \text{ mW/m}^2$  invoked as representative of Mesozoic-Cenozoic rifts for  
496 Antarctic ice sheet modelling (Pollard et al., 2005). A slightly higher heat flow of  
497  $\sim 75 \text{ mW/m}^2$  at BYRD was estimated from a drill core through the ice sheet to  
498 bedrock (Gow et al., 1968). These values contrast with inferred heat flows in the  
499 central WARS of  $\sim >120 \text{ mW/m}^2$  based on airborne magnetic data (Martos et al.,  
500 2017) and  $\sim 110 \text{ mW/m}^2$  based on the extrapolation of global heat flow measurements  
501 to Antarctica via seismic structural similarity (Shapiro & Ritzwoller, 2004).

502 Our preferred heat flow of  $\sim 60 \text{ mW/m}^2$  at PIG3 is broadly consistent with infer-  
503 ences from satellite magnetic data ( $\sim 55\text{-}65 \text{ mW/m}^2$ ; Fox Maule et al., 2005), seismic  
504 data ( $\sim 70 \text{ mW/m}^2$ ; An et al., 2015a), airborne magnetic data ( $\sim 60\text{-}75 \text{ mW/m}^2$ ; Mar-  
505 tos et al., 2017), and in situ measurements in continental shelf sediments in the  
506 Amundsen Sea Embayment (mean  $\sim 65 \text{ mW/m}^2$ ; Dziadek et al., 2019). Our preferred  
507  $\sim 60 \text{ mW/m}^2$  heat flow at PIG3 again contrasts with the  $\sim 110 \text{ mW/m}^2$  modelled by

508 Shapiro & Ritzwoller (2004); however, their modelled standard deviations are of com-  
509 parable magnitude to their inferred heat flows.

510 Our preferred heat flow of  $\sim 50 \text{ mW/m}^2$  at node 1624 in the Ellsworth Mountains  
511 is lower than estimates based on satellite magnetic data ( $\sim 70 \text{ mW/m}^2$ ; Fox Maule  
512 et al., 2005) and airborne magnetic data ( $\sim 65\text{-}70 \text{ mW/m}^2$ ; Martos et al., 2017), but  
513 reasonably consistent with recent seismic-based inferences ( $\sim 55 \text{ mW/m}^2$ ; An et al.,  
514 2015a). High heat producing granites in the upper crust are known to occur in the  
515 Ellsworth Mountains (e.g., Leat et al., 2018), a factor which might render the partition  
516 model of heat production with  $F = 0.74$  inappropriate for modelling the local thermal  
517 regime.

518 A surface heat flow of  $\sim 60 \text{ mW/m}^2$  best explains the observed  $V_{SV}$  profiles at BREN.  
519 The signature of a clear seismic LAB at BREN is lacking, likely a reflection of the  
520 degradation in resolution at the model periphery, but  $q_S = 60 \text{ mW/m}^2$  gives a thermal  
521 LAB of  $\sim 85 \text{ km}$ . Burton-Johnson et al. (2017) used geological analyses to infer a mean  
522 heat flow of  $81 \text{ mW/m}^2$  on the east and south of the Antarctic Peninsula where silicic  
523 rocks predominate, and a mean of  $67 \text{ mW/m}^2$  on the west and north where volcanic  
524 arc and quartzose sediments dominate. BREN is located approximately on the border  
525 between these domains, where the heat flow inferred by Burton-Johnson et al. (2017)  
526 is  $\sim 60\text{-}80 \text{ mW/m}^2$ . Martos et al. (2017) broadly replicate the spatial variation in heat  
527 flow on the Peninsula, but their inferred values are consistently higher than those of  
528 Burton-Johnson et al. (2017).

529 We emphasise that inferred heat flows are regional average (many hundreds of km)  
530 estimates constrained by seismic data with limited sensitivity to the upper crust in  
531 conjunction with radiogenic heat productions for felsic, mafic and ultramafic litholo-  
532 gies taken from global compilations (e.g., Hasterok & Chapman, 2011; Furlong &  
533 Chapman, 2013). This precludes meaningful comparison with geographically localised  
534 high heat flow anomalies (e.g., Fisher et al., 2015), but does not contradict such mea-

535 surements. Our inferred geotherms and heat flows can serve as regional average  
536 benchmarks which can be modified according to local conditions.

## 537 **7 Conclusions**

538 In this work, we combined data from the UKANET, POLENET-ANET, ASAIN,  
539 SEPA and GSN seismic arrays to construct from fundamental mode Rayleigh wave  
540 phase velocities a 3D shear wave velocity model of the West Antarctic upper mantle to  
541 200 km depth. Our goals were (i) image and interpret structures against the tectonic  
542 evolution of West Antarctica, and (ii) extract information from the seismic model  
543 that can serve as boundary conditions in ice sheet and GIA modelling efforts.

544 We speculate that a high velocity anomaly located in the southern WSRS might reflect  
545 depleted mantle lithosphere following the extraction of voluminous melt related to  
546 Gondwana fragmentation. High velocity anomalies imaged by body-wave tomography  
547 in the upper mantle beneath the eastern Ross Sea Embayment have been interpreted  
548 as lithosphere that may not have been reheated by the Cenozoic rifting that affected  
549 other parts of the WARS (White-Gaynor et al., 2019). Motivated by xenolith analyses,  
550 as an alternative model we propose that high velocity zones imaged south of the  
551 MBL dome and in the eastern Ross Sea Embayment in this study might reflect the  
552 compositional signature of ancient continental fragments.

553 While the seismic signature of the cratonic margin of East Antarctic is clear along  
554 the southern and northern TAM, the absence of a sharp velocity contrast between  
555 the WSRS and East Antarctica is consistent with the WSRS being a broad exten-  
556 sional/transensional province within a distributed plate boundary between East and  
557 West Antarctica (Jordan et al., 2017).

558 A pronounced low velocity anomaly underlying the southern TAM is consistent with a  
559 published lithospheric foundering hypothesis. Taken together with a magnetotelluric



560 study advocating flexural support of the central TAM by thick, stable lithosphere  
561 (Wannamaker et al., 2017), this points to along-strike variation in the tectonic history  
562 of the TAM.

563 The Bentley Subglacial Trench aside - which may have experienced a pulse of Neogene  
564 extension (Lloyd et al., 2015) - the distribution of low velocity anomalies suggests that  
565 current tectonism in the WARS is concentrated beneath the rift margins and largely  
566 confined to the uppermost mantle (<180 km depth). On the northern margin of the  
567 WARS, a pronounced low velocity anomaly extends eastward from beneath the MBL  
568 dome toward Pine Island Bay. If of plume-related thermal origin, the velocity con-  
569 trast of  $\sim 5\%$  between this anomaly and the inner WARS translates to a temperature  
570 difference of  $\sim 125\text{-}200^\circ\text{C}$ . However, the strike of the anomaly parallels the paleo-  
571 Pacific convergent margin of Gondwana, so it conceivably encodes the signature of  
572 subduction-related melt and volatiles rather than anomalously elevated temperatures,  
573 or a combination thereof. Thermal versus chemical origins will have different impli-  
574 cations for geothermal heat flow and mantle viscosity modelling efforts to monitor  
575 and predict ice sheet evolution. Differentiating between them should be a pressing  
576 concern given that the anomaly underlies Thwaites Glacier, a major outlet glacier of  
577 the WAIS considered vulnerable to marine ice sheet instability (e.g., Barletta et al.,  
578 2018).

579 Lithospheric thickness estimates extracted from 1D shear wave velocity profiles rep-  
580 resentative of tectonic domains in West Antarctica indicate an average lithospheric  
581 thickness of  $\sim 85$  km for the WARS, MBL, and Thurston Island block. This in-  
582 creases to  $\sim 96$  km in the Ellsworth Mountains.  $\sim 60$  mW/m<sup>2</sup> geotherms best explain  
583 lithospheric mantle shear wave velocities in the central WARS (BYRD) and adja-  
584 cent to Pine Island Glacier in the Thurston Island block (PIG3); a  $\sim 50$  mW/m<sup>2</sup>  
585 geotherm best explains the velocities in the Ellsworth Mountains (node 1624) and  
586 a  $\sim 60$  mW/m<sup>2</sup> geotherm best explains a less well-constrained velocity profile on the

587 southern Antarctic Peninsula (1624). We emphasise that inferred heat flows are re-  
588 gional average estimates constrained by seismic data with limited sensitivity to the  
589 upper crust. They do not preclude geographically-localised elevated heat flows due  
590 to localised Cenozoic extension or magmatic activity or variations in upper crustal  
591 heat production rooted in compositional variation.

## 592 **8 Acknowledgements**

593 We thank all BAS camp staff, field guides and air unit personnel for the logistical  
594 support of the UKANET seismic and GNSS networks. We similarly acknowledge  
595 all field teams and camp staff associated with the POLENET-ANET project, and  
596 thank Kenn Borek Air and the New York Air Guard for flight support. JPOD,  
597 GAN and PLW are supported by the Natural Environment Research Council [grants  
598 NE/L006065/1, NE/L006294/1 and NE/K009958/1], KS is supported by the Aus-  
599 tralia Research Council [grant F150100541]. POLENET-ANET is supported by the  
600 National Science Foundation Office of Polar Programs [grants 0632230, 0632239,  
601 0652322, 0632335, 0632136, 0632209, and 0632185]. UKANET seismic instrumen-  
602 tation was provided and supported by SEIS-UK. POLENET-ANET seismic instru-  
603 mentation was provided and supported by the Incorporated Research Institutions  
604 for Seismology (IRIS) through the PASSCAL Instrument Center. The UKANET  
605 ([www.ukanet.wixsite.com/ukanet](http://www.ukanet.wixsite.com/ukanet); network code 1D; [https://doi.org/10.7914/](https://doi.org/10.7914/SN/1D_2016)  
606 [SN/1D\\_2016](https://doi.org/10.7914/SN/1D_2016)) data will be accessible through the IRIS Data Management Center  
607 (<http://www.iris.edu/mda>) from January 2021. POLENET-ANET (network code  
608 YT), ASAIN (network code AI), GSN (network code IU) and SEPA (network code  
609 XB) seismic data can be accessed through the IRIS DMC. The facilities of the IRIS  
610 Consortium are supported by the NSF under cooperative agreement EAR-1063471,  
611 the NSF Office of Polar Programs, and the DOE National Nuclear Security Admin-

612 istration. Figures were created using the Generic Mapping Tools (GMT) software  
613 (<http://gmt.soest.hawaii.edu>). The phase and shear wave velocity models de-  
614 veloped here can be accessed at the UK Polar Data Centre ([https://doi.org/10.](https://doi.org/10.5285/c11bdb27-df44-4b56-8f4c-afc51b6e1e3a)  
615 [5285/c11bdb27-df44-4b56-8f4c-afc51b6e1e3a](https://doi.org/10.5285/c11bdb27-df44-4b56-8f4c-afc51b6e1e3a) and [https://doi.org/10.5285/](https://doi.org/10.5285/b5ffac8a-9846-4f86-9a71-3ce992a18148)  
616 [b5ffac8a-9846-4f86-9a71-3ce992a18148](https://doi.org/10.5285/b5ffac8a-9846-4f86-9a71-3ce992a18148)).

## 617 **References**

- 618 Abers, G. A. & Hacker, B. R., 2016. A MATLAB toolbox and Excel workbook  
619 for calculating the densities, seismic wave speeds, and major element composition  
620 of minerals and rocks at pressure and temperature, *Geochem. Geophys. Geosyst.*,  
621 **17**(2), 616–624, doi:10.1002/2015GC006171.
- 622 An, M., Wiens, D. A., Zhao, Y., Feng, M., Nyblade, A., Kanao, M., Li, Y., Maggi, A.,  
623 & L ev eque, J.-J., 2015a. Temperature, lithosphere-asthenosphere boundary, and  
624 heat flux beneath the Antarctic Plate inferred from seismic velocities, *J. Geophys.*  
625 *Res.*, **120**(12), 8720–8742, doi:10.1002/2015JB011917.
- 626 An, M., Wiens, D. A., Zhao, Y., Feng, M., Nyblade, A. A., Kanao, M., Li, Y.,  
627 Maggi, A., & L ev eque, J.-J., 2015b. S-velocity model and inferred Moho topography  
628 beneath the Antarctic Plate from Rayleigh waves, *J. Geophys. Res.*, **120**(1), 359–  
629 383.
- 630 Barletta, V. R., Bevis, M., Smith, B. E., Wilson, T., Brown, A., Bordoni, A., Willis,  
631 M., Khan, S. A., Rovira-Navarro, M., Dalziel, I., Smalley, R., Kendrick, E., Konfal,  
632 S., Caccamise, D. J., Aster, R. C., Nyblade, A., & Wiens, D. A., 2018. Observed  
633 rapid bedrock uplift in Amundsen Sea Embayment promotes ice-sheet stability,  
634 *Science*, **360**(6395), 1335–1339, doi:10.1126/science.aao1447.
- 635 Birch, F., 1961. The velocity of compressional waves in rocks to 10 kilobars, part 2,  
636 *J. Geophys. Res.*, **66**(7), 2199–2224.
- 637 Brocher, T. M., 2005. Empirical Relations between Elastic Wavespeeds and Density  
638 in the Earth’s Crust, *Bull., Seis. Soc. Am.*, **95**(6), 2081.
- 639 Burton-Johnson, A., Halpin, J. A., Whittaker, J. M., Graham, F. S., & Watson, S. J.,  
640 2017. A new heat flux model for the Antarctic Peninsula incorporating spatially

641 variable upper crustal radiogenic heat production, *Geophys. Res. Lett.*, **44**(11),  
642 5436–5446, doi:10.1002/2017GL073596.

643 Chaput, J., Aster, R. C., Huerta, A., Sun, X., Lloyd, A., Wiens, D., Nyblade, A.,  
644 Anandakrishnan, S., Winberry, J. P., & Wilson, T., 2014. The Crustal Thickness  
645 of West Antarctica, *J. Geophys. Res.*, **119**, 1–18, doi:10.1002/2013JB010642.

646 Dalziel, I. W. D., 1992. Antarctica: A tale of two supercontinents?, *Annu. Rev. Earth*  
647 *Pl. Sc.*, **20**, 501–526.

648 Dalziel, I. W. D. & Elliot, D. H., 1982. West Antarctica: Problem child of Gond-  
649 wanaland, *Tectonics*, **1**(1), 3–19, doi:10.1029/TC001i001p00003.

650 Dziadek, R., Gohl, K., Kaul, N., & Science Team of Expedition PS1041, 2019. Ele-  
651 vated geothermal surface heat flow in the Amundsen Sea Embayment, West Antarc-  
652 tica, *Earth Planet. Sci. Lett.*, **506**, 530–539, doi:10.1016/j.epsl.2018.11.003.

653 Dziewonski, A. M. & Anderson, D. L., 1981. Preliminary reference Earth model,  
654 *Phys. Earth Planet. Int.*, **25**(4), 297–356.

655 Eaton, D. W., Darbyshire, F., Evans, R. L., Grütter, H., Jones, A. G., & Yuan,  
656 X., 2009. The elusive lithosphere-asthenosphere boundary (LAB) beneath cratons,  
657 *Lithos*, **109**(1-2), 1–22.

658 Emry, E. L., Nyblade, A. A., Julià, J., Anandakrishnan, S., Aster, R. C., Wiens,  
659 D. A., Huerta, A. D., & Wilson, T. J., 2014. The mantle transition zone beneath  
660 West Antarctica: Seismic evidence for hydration and thermal upwellings, *Geochem.*  
661 *Geophys. Geosyst.*, **16**(1), 40–58, doi:10.1002/2014GC005588.

662 Faul, U. H. & Jackson, I., 2005. The seismological signature of temperature and grain  
663 size variations in the upper mantle, *Earth Planet. Sci. Lett.*, **234**, 119–134.

- 664 Finn, C. A., Müller, R. D., & Panter, K. S., 2005. A Cenozoic diffuse alkaline  
665 magmatic province (DAMP) in the southwest Pacific without rift or plume origin,  
666 *Geochem. Geophys. Geosyst.*, **6**(2), doi:10.1029/2004GC000723.
- 667 Fisher, A. T., Mankoff, K. D., Tulaczyk, S. M., Tyler, S. W., Foley, N., & the  
668 WISSARD science team, 2015. High geothermal heat flux measured below the  
669 West Antarctic Ice Sheet, *Sci. Adv.*, **1**(6), doi:10.1126/sciadv.1500093.
- 670 Fitzgerald, P., 2002. Tectonics and landscape evolution of the Antarctic plate since  
671 the breakup of Gondwana, with an emphasis on the West Antarctic Rift System  
672 and the Transantarctic Mountains, *Royal Society of New Zealand Bulletin*, **35**,  
673 453–469.
- 674 Forysth, D. W. & Li, A., 2005. Array analysis of two-dimensional variations in sur-  
675 face wave phase velocity and azimuthal anisotropy in the presence of multipathing  
676 interference, in Seismic Earth: Array Analysis of Broadband Seismograms, Geo-  
677 phys. Monogr. Ser. 157, pp. 81–97, eds Levander, A. & Nolet, G., American Geo-  
678 physical Union, Washington, DC, doi:10.1029/157GM06.
- 679 Fox Maule, C., Purucker, M. E., Olsen, N., & Mosegaard, K., 2005. Heat Flux  
680 Anomalies in Antarctica Revealed by Satellite Magnetic Data, *Science*, **309**(5733),  
681 464–467.
- 682 Fretwell, P., Pritchard, H. D., Vaughan, D. G., Bamber, J. L., Barrand, N. E., Bell, R.,  
683 Bianchi, C., Bingham, R. G., Blankenship, D. D., Casassa, G., Catania, G., Callens,  
684 D., Conway, H., Cook, A. J., Corr, H. F. J., Damaske, D., Damm, V., Ferraccioli, F.,  
685 Forsberg, R., Fujita, S., Gim, Y., Gogineni, P., Griggs, J. A., Hindmarsh, R. C. A.,  
686 Holmlund, P., Holt, J. W., Jacobel, R. W., Jenkins, A., Jokat, W., Jordan, T.,  
687 King, E. C., Kohler, J., Krabill, W., Riger-Kusk, M., Langley, K. A., Leitchenkov,  
688 G., Leuschen, C., Luyendyk, B. P., Matsuoka, K., Mouginot, J., Nitsche, F. O.,

689 Nogi, Y., Nost, O. A., Popov, S. V., Rignot, E., Rippin, D. M., Rivera, A., Roberts,  
690 J., Ross, N., Siegert, M. J., Smith, A. M., Steinhage, D., Studinger, M., Sun, B.,  
691 Tinto, B. K., Welch, B. C., Wilson, D., Young, D. A., Xiangbin, C., & Zirizzotti, A.,  
692 2013. Bedmap2: improved ice bed, surface and thickness datasets for Antarctica,  
693 *The Cryosphere*, **7**, 375–393, doi:10.5194/tc-7-375-2013.

694 Furlong, K. P. & Chapman, D. S., 2013. Heat Flow, Heat Generation, and the  
695 Thermal State of the Lithosphere, *Annu. Rev. Earth Pl. Sc.*, **41**(1), 385–410,  
696 doi:10.1146/annurev.earth.031208.100051.

697 Gow, A. J., Ueda, H. T., & Garfield, D. E., 1968. Antarctic ice sheet: Preliminary  
698 results of first core hole to bedrock, *Science*, **161**(3845), 1011–1013.

699 Griffin, W. L., O'Reilly, S. Y., Afonso, J. C., & Begg, G. C., 2009. The Composition  
700 and Evolution of Lithospheric Mantle: a Re-evaluation and its Tectonic Implica-  
701 tions, *J. Petrol.*, **50**(7), 1185–1204, doi:10.1093/petrology/egn033.

702 Guo, Z., Chen, Y. J., Ning, J., Yang, Y., Afonso, J. C., & Tang, Y., 2016. Seismic evi-  
703 dence of on-going sublithosphere upper mantle convection for intra-plate volcanism  
704 in Northeast China, *Earth Planet. Sci. Lett.*, **433**, 31–43.

705 Hacker, B. R., Kelemen, P. B., & Behn, M. D., 2015. Continental lower crust, *Annual*  
706 *Review of Earth and Planetary Sciences*, **43**(1), 167–205, doi:10.1146/annurev-  
707 earth-050212-124117.

708 Handler, M. R., Wysoczanski, R. J., & Gamble, J. A., 2003. Proterozoic lithosphere  
709 in Marie Byrd Land, West Antarctica: Re-Os systematics of spinel peridotite xeno-  
710 liths, *Chem. Geol.*, **196**(1-4), 131–145, doi:10.1016/S0009-2541(02)00410-2.

711 Hasterok, D. & Chapman, D., 2011. Heat production and geotherms  
712 for the continental lithosphere, *Earth Planet. Sci. Lett.*, **307**(1), 59–70,  
713 doi:10.1016/j.epsl.2011.04.034.

- 714 Heeszel, D. S., Wiens, D. A., Anandakrishnan, S., Aster, R. C., Dalziel, I. W. D.,  
715 Huerta, A. D., Nyblade, A. A., Wilson, T. J., & Winberry, P., 2016. Upper mantle  
716 structure of central and West Antarctica from array analysis of Rayleigh wave phase  
717 velocities, *J. Geophys. Res.*, doi:10.1002/2015JB012616.
- 718 Jordan, T., Ferraccioli, F., & Leat, P., 2017. New geophysical compilations  
719 link crustal block motion to Jurassic extension and strike-slip faulting in the  
720 Weddell Sea Rift System of West Antarctica, *Gondwana Research*, **42**, 29–48,  
721 doi:10.1016/j.gr.2016.09.009.
- 722 Katsura, T., Yoneda, A., Yamazaki, D., Yoshino, T., & Ito, E., 2010. Adiabatic  
723 temperature profile in the mantle, *Phys. Earth Planet. Int.*, **183**(1-2), 212–218,  
724 doi:10.1016/j.pepi.2010.07.001.
- 725 Lawrence, J. F., Wiens, D. A., Nyblade, A. A., Anandakrishnan, S., Shore, P.,  
726 & Voigt, D., 2006. Crust and upper mantle structure of the Transantarctic  
727 Mountains and surrounding regions from receiver functions, surface waves,  
728 and gravity: Implications for uplift models, *Geochem. Geophys. Geosyst.*, **7**(10),  
729 doi:10.1029/2006GC001282.
- 730 Leat, P. T., Jordan, T. A., Flowerdew, M. J., Riley, T. R., Ferraccioli, F., &  
731 Whitehouse, M. J., 2018. Jurassic high heat production granites associated  
732 with the Weddell Sea rift system, Antarctica, *Tectonophysics*, **722**, 249–264,  
733 doi:10.1016/j.tecto.2017.11.011.
- 734 Lee, C.-T. A., 2003. Compositional variation of density and seismic velocities  
735 in natural peridotites at STP conditions: Implications for seismic imaging of  
736 compositional heterogeneities in the upper mantle, *J. Geophys. Res.*, **108**(B9),  
737 doi:10.1029/2003JB002413.
- 738 LeMasurier, W. E. & Landis, C. A., 1996. Mantle-plume activity recorded by low-



- 739 relief erosion surfaces in West Antarctica and New Zealand, *Geol. Soc. Am. Bull.*,  
740 **108**(11), 1450–1466.
- 741 Liu, J., Scott, J. M., Martin, C. E., & Pearson, D. G., 2015. The longevity of Archean  
742 mantle residues in the convecting upper mantle and their role in young continent  
743 formation, *Earth Planet. Sci. Lett.*, **424**, 109–118, doi:10.1016/j.epsl.2015.05.027.
- 744 Lloyd, A. J., Wiens, D. A., Nyblade, A. A., Anandakrishnan, S., Aster, R. C., Huerta,  
745 A. D., Wilson, T. J., Dalziel, I. W. D., Shore, P. J., & Zhao, D., 2015. A seismic  
746 transect across West Antarctica: Evidence for mantle thermal anomalies beneath  
747 the Bentley Subglacial Trench and the Marie Byrd Land Dome, *J. Geophys. Res.*,  
748 **120**(12), 8439–8460, doi:10.1002/2015JB012455.
- 749 Martos, Y. M., Catalán, M., Jordan, T. A., Golynsky, A., Golynsky, D., Eagles, G.,  
750 & Vaughan, D. G., 2017. Heat Flux Distribution of Antarctica Unveiled, *Geophys.*  
751 *Res. Lett.*, **44**(22), 11,417–11,426, doi:10.1002/2017GL075609.
- 752 McDonough, W., 1990. Constraints on the composition of the continental lithospheric  
753 mantle, *Earth Planet. Sci. Lett.*, **101**(1), 1–18, doi:10.1016/0012-821X(90)90119-I.
- 754 Nield, G. A., Whitehouse, P. L., van der Wal, W., Blank, B., O'Donnell, J. P., &  
755 Stuart, G. W., 2018. The impact of lateral variations in lithospheric thickness on  
756 glacial isostatic adjustment in West Antarctica, *Geophys. J. Int.*, **214**(2), 811–824,  
757 doi:10.1093/gji/ggy158.
- 758 O'Donnell, J. P. & Nyblade, A. A., 2014. Antarctica's hypsometry and crustal thick-  
759 ness: Implications for the origin of anomalous topography in East Antarctica, *Earth*  
760 *Planet. Sci. Lett.*, **388**, 143–155.
- 761 O'Donnell, J. P., Selway, K., Nyblade, A. A., Brazier, R. A., Wiens, D. A., Anandakr-  
762 ishnan, S., Aster, R. C., Huerta, A. D., Wilson, T., & Winberry, J. P., 2017. The

- 763 uppermost mantle seismic velocity and viscosity structure of central West Antarc-  
764 tica, *Earth Planet. Sci. Lett.*, **472**, 38–49, doi:10.1016/j.epsl.2017.05.016.
- 765 O’Donnell, J. P., Dunham, C., Stuart, G. W., Brisbourne, A., Nield, G. A., White-  
766 house, P. L., Hooper, A. J., Nyblade, A., Wiens, D., Aster, R. C., Anandakrishnan,  
767 S., Huerta, A. D., Wilson, T. J., & Winberry, J. P., 2018. Geothermal Heat Flux  
768 and Upper Mantle Viscosity across West Antarctica: Insights from the UKANET  
769 and POLENET Seismic Networks, *AGU Fall Meeting Abstracts*.
- 770 Pollard, D., DeConto, R. M., & Nyblade, A. A., 2005. Sensitivity of Cenozoic Antarc-  
771 tic ice sheet variations to geothermal heat flux, *Glob. Planet. Change*, **49**(1-2),  
772 63–74.
- 773 Ramirez, C., Nyblade, A., Emry, E., Julià, J., Sun, X., Anandakrishnan, S., Wiens,  
774 D., Aster, R., Huerta, A., Winberry, P., & Wilson, T., 2017. Crustal structure of the  
775 Transantarctic Mountains, Ellsworth Mountains and Marie Byrd Land, Antarctica:  
776 constraints on shear wave velocities, Poisson’s ratios and Moho depths, *Geophys.*  
777 *J. Int.*, **211**(3), 1328–1340.
- 778 Ritzwoller, M. H., Shapiro, N. M., Levshin, A. L., & Leahy, G. M., 2001. Crustal and  
779 upper mantle structure beneath Antarctica and surrounding oceans, *J. Geophys.*  
780 *Res.*, **106**(B12), 30645–30670, doi:10.1029/2001JB000179.
- 781 Shapiro, N. M. & Ritzwoller, M. H., 2004. Inferring surface heat flux distribu-  
782 tions guided by a global seismic model: particular application to Antarctica, *Earth*  
783 *Planet. Sci. Lett.*, **223**(1), 213–224, doi:10.1016/j.epsl.2004.04.011.
- 784 Shen, W., Wiens, D. A., Stern, T., Anandakrishnan, S., Aster, R. C., Dalziel, I.,  
785 Hansen, S., Heeszel, D. S., Huerta, A., Nyblade, A., Wilson, T. J., & Winberry,  
786 J. P., 2017. Seismic evidence for lithospheric foundering beneath the southern  
787 Transantarctic Mountains, Antarctica, *Geology*, **46**(1), 71, doi:10.1130/G39555.1.

- 788 Shen, W., Wiens, D. A., Anandakrishnan, S., Aster, R. C., Gerstoft, P., Bromirski,  
789 P. D., Hansen, S. E., Dalziel, I. W. D., Heeszel, D. S., Huerta, A. D., Nyblade, A. A.,  
790 Stephen, R., Wilson, T. J., & Winberry, J. P., 2018. The Crust and Upper Mantle  
791 Structure of Central and West Antarctica From Bayesian Inversion of Rayleigh  
792 Wave and Receiver Functions, *J. Geophys. Res.*, doi:10.1029/2017JB015346.
- 793 Storey, B. & Kyle, P., 1997. An active mantle mechanism for Gondwana breakup, *S.*  
794 *Afr. J. Geol.*, **100**(4), 283–290.
- 795 van Wijk, J., Lawrence, J., & Driscoll, N., 2008. Formation of the Transantarctic  
796 Mountains related to extension of the West Antarctic Rift system, *Tectonophysics*,  
797 **458**(1), 117–126, doi.org/10.1016/j.tecto.2008.03.009.
- 798 Vaughan, A. P. M., Kelley, S. P., & Storey, B. C., 2002. Mid-Cretaceous ductile  
799 deformation on the Eastern Palmer Land Shear Zone, Antarctica, and im-  
800 plications for timing of Mesozoic terrane collision, *Geol. Mag.*, **139**(4), 465–471,  
801 doi:10.1017/S0016756802006672.
- 802 Wannamaker, P., Hill, G., Stodt, J., Maris, V., Ogawa, Y., Selway, K., Boren, G.,  
803 Bertrand, E., Uhlmann, D., Ayling, B., Green, A. M., & Feucht, D., 2017. Uplift  
804 of the central transantarctic mountains, *Nat. Commun.*, **8**(1), 1588.
- 805 White-Gaynor, A. L., Nyblade, A. A., Aster, R. C., Wiens, D. A., Bromirski,  
806 P. D., Gerstoft, P., Stephen, R. A., Hansen, S. E., Wilson, T., Dalziel, I. W.,  
807 Huerta, A. D., Winberry, J. P., & Anandakrishnan, S., 2019. Heterogeneous upper  
808 mantle structure beneath the Ross Sea Embayment and Marie Byrd Land, West  
809 Antarctica, revealed by P-wave tomography, *Earth Planet. Sci. Lett.*, **513**, 40–50,  
810 doi:10.1016/j.epsl.2019.02.013.
- 811 Yang, Y. & Forsyth, D. W., 2006. Regional tomographic inversion of the amplitude

812 and phase of Rayleigh waves with 2-D sensitivity kernels, *Geophys. J. Int.*, **166**,  
813 1148–1160.

# Figures

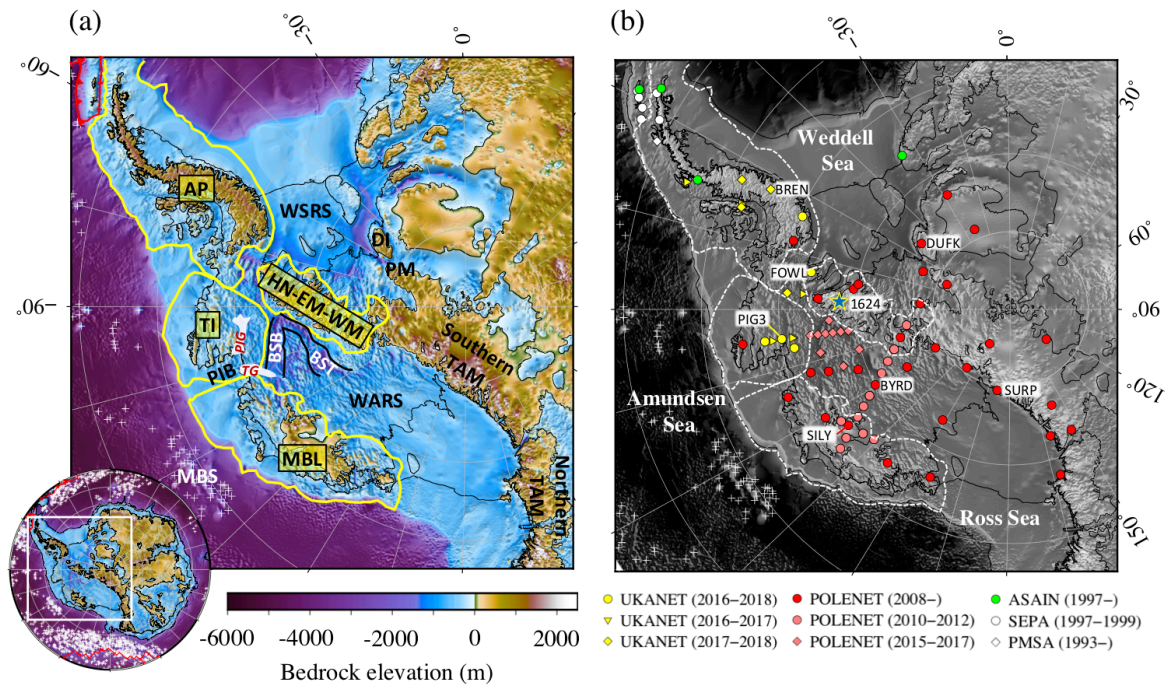


Figure 1: (a) Map of West Antarctic BEDMAP2 bedrock topography (Fretwell et al., 2013). Following Dalziel & Elliot (1982), yellow lines delineate the major crustal blocks of West Antarctica that pre-date Gondwana fragmentation (AP, Antarctic Peninsula; TI, Thurston Island; MBL, Marie Byrd Land; HN-EM-WM, Haag Nunataks-Ellsworth Whitmore Mountains Block, hereafter HEW). The approximate locations of Pine Island Glacier (PIG) and Thwaites Glacier (TG) in the Amundsen Sea Embayment are outlined in white. Plate boundaries are marked in red and white crosses show the locations of seamounts. Other abbreviated geographic features: BSB, Byrd Subglacial Basin; BST, Bentley Subglacial Trench; DI, Dufek Intrusion; MBS, Marie Byrd Seamounts; PIB, Pine Island Bay; PM, Pensacola Mountains; TAM, Transantarctic Mountains; WARS, West Antarctic Rift System; WSRs, Weddell Sea Rift System. (b) Map showing the location of the UKANET, POLENET-ANET, ASAIN, SEPA and GSN seismic stations used in this study superimposed on grey-scale bedrock topography. At initial deployment in January-February 2016, five UKANET seismic stations were arranged in a quasi-linear array straddling Pine Island Glacier, two stations were located approximately north of the HEW block, and three stations were deployed along the southern Antarctica Peninsula. At the end of the first year of the deployment the UKANET array was re-configured to bolster coverage along the southern Antarctic Peninsula. The UKANET seismic array was demobilised in January-February 2018. Specific stations and grid nodes (blue star) referred to in the text are labelled. For interpretation of the references to colour in this figure, the reader is referred to the web version of the article.

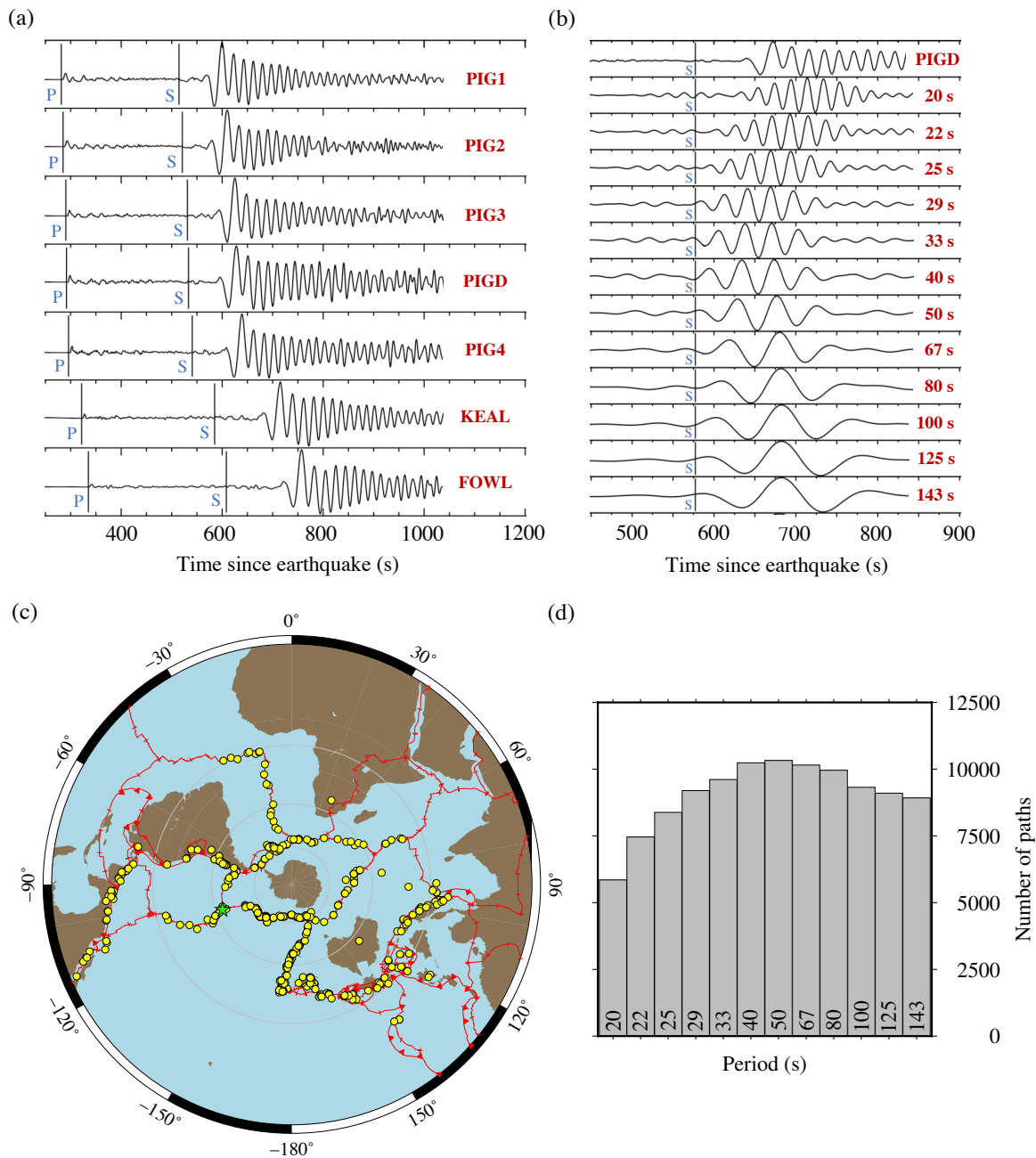


Figure 2: (a) Vertical-component seismograms from a magnitude 6.0 East Pacific Rise earthquake that occurred on August 18<sup>th</sup> 2016 (green star in (c)) recorded at seven UKANET seismic stations in West Antarctica (see Table S1). Predicted arrival times of compressional (P) and shear (S) body waves according to the Preliminary Reference Earth Model (PREM; Dziewonski & Anderson, 1981) are marked, after which follows the larger amplitude Rayleigh wave. (b) Rayleigh wave dispersion of the same earthquake at UKANET station PIGD. The raw Rayleigh wave seismogram (top) is filtered into 12  $\times$  10 mHz wide frequency bands with centre periods ranging from 20 to 143 s. (c) Azimuthal and epicentral distance distribution of the 457 earthquakes used in this study. Tomographic resolution is enhanced by a uniform azimuthal distribution of earthquakes. Concentric circles are at 30° intervals from the south pole. (d) Total number of ray paths used at each period in this study.

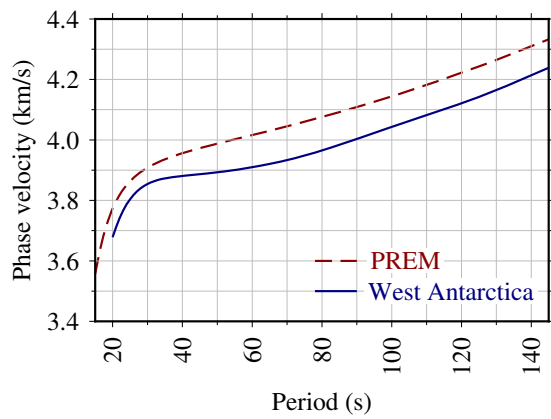


Figure 3: Average Rayleigh wave phase velocity dispersion curve for West Antarctica compared with PREM. The 1D average dispersion curve served as a starting model for subsequent 2D tomographic phase velocity inversions.



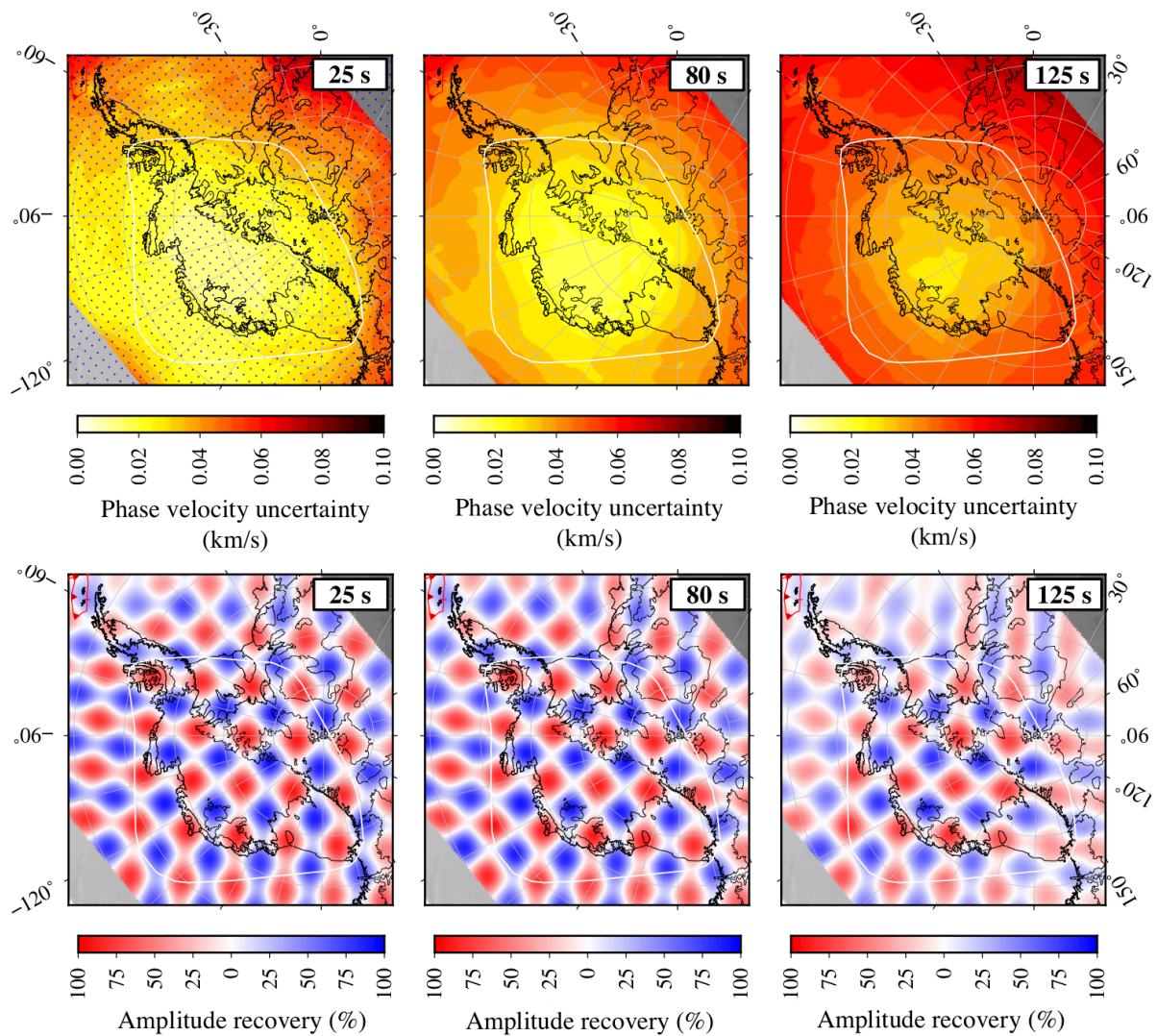


Figure 4: (Top) Rayleigh wave phase velocity model uncertainty at periods 25, 80 and 125 s. Grid node locations are superimposed on the 25 s map. (Bottom) Rayleigh wave phase velocity model resolution at corresponding periods. For ease of visualization, we present the resolution matrix multiplied by a checkerboard pattern of phase velocity anomalies of wavelength 400 km. 100% represents complete amplitude recovery of positive/negative velocity anomalies. We confine our subsequent discussion of imaged structure to the region enclosed by the white polygon.

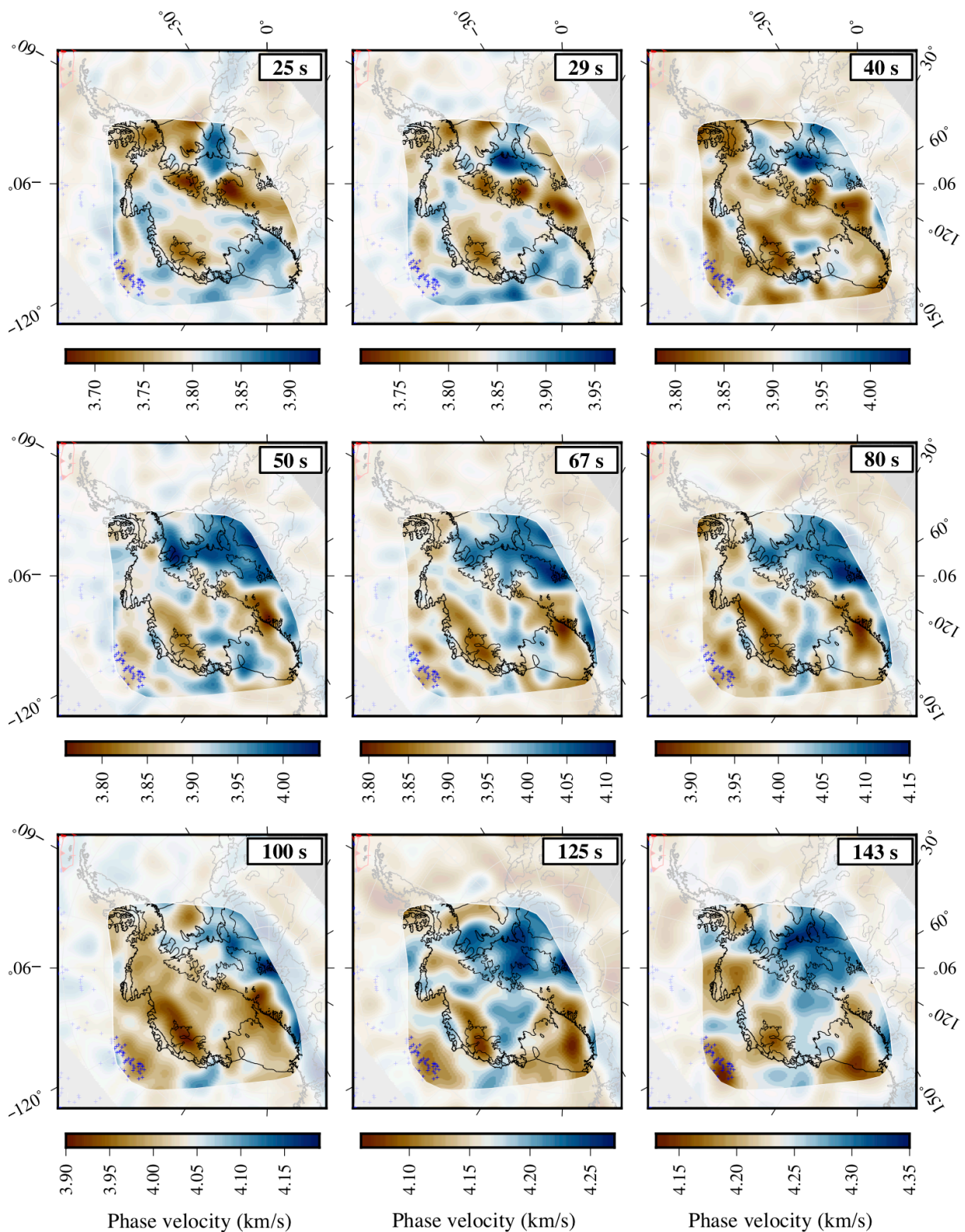


Figure 5: Rayleigh wave phase velocity model at a range of periods. Unique scale bars are used at each period to emphasise lateral velocity variations. Blue crosses show the locations of seamounts. Regions of higher uncertainty and lower resolution are masked.

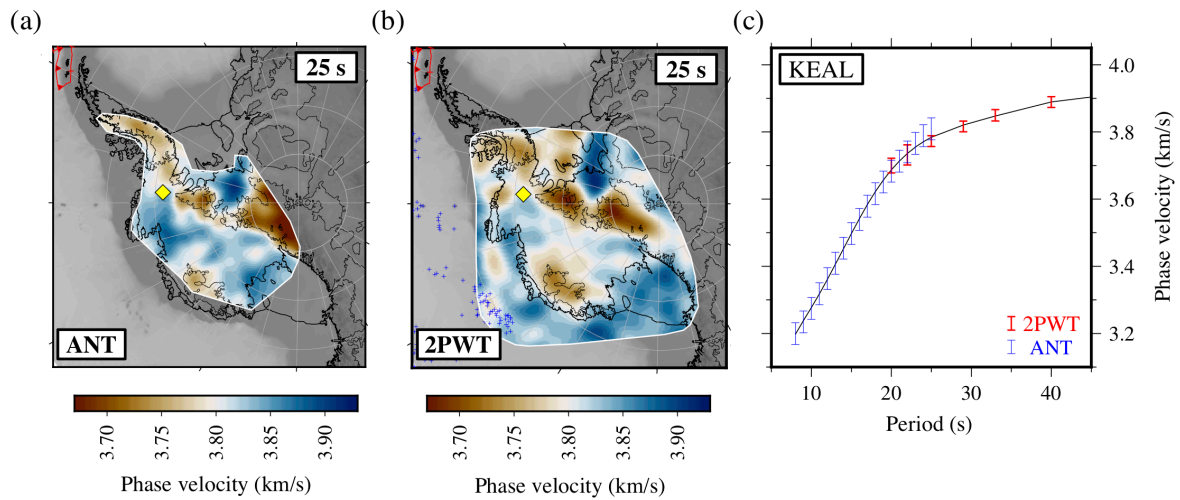


Figure 6: Comparison of Rayleigh wave phase velocity maps at period 25 s inferred by (a) ambient noise tomography (ANT; period range 8-25 s) and (b) two-plane-wave tomography (2PWT; period range 20-143 s). (c) Composite 8-143 s Rayleigh wave phase velocity dispersion curve for UKANET station KEAL obtained by weighted least squares polynomial regression (black curve) of ANT- and 2PWT-curves. The yellow diamond in (a) and (b) shows the location of KEAL.

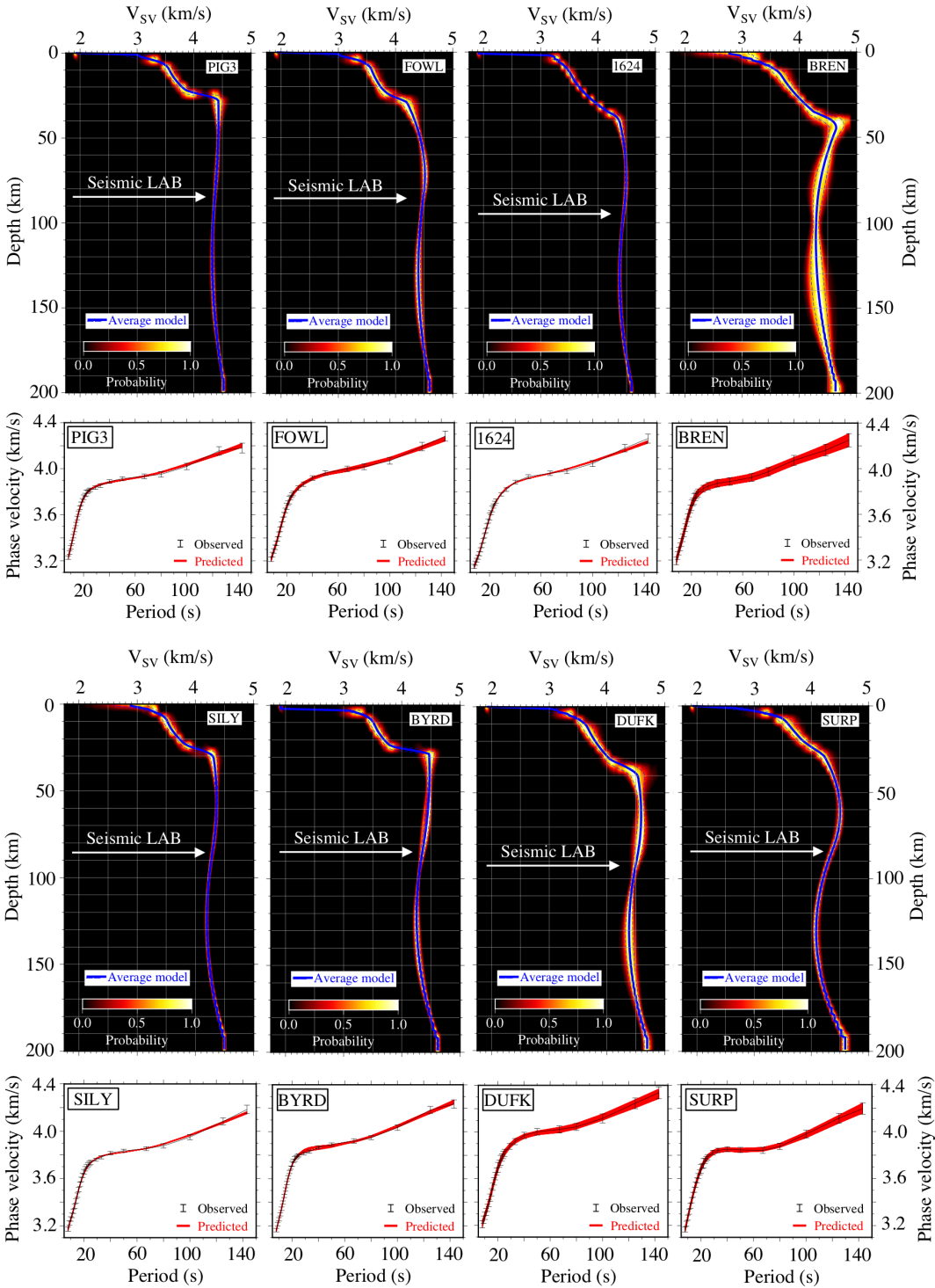


Figure 7: Vertically-polarised shear wave velocity ( $V_{SV}$ ) profiles inferred from corresponding Rayleigh wave phase velocity dispersion curves. The thick blue line is the mean  $V_{SV}$  velocity, the blue dashed lines are one standard deviation bounds. 0 km depth corresponds to the local elevation of the ice sheet surface at each location. The seismic lithosphere-asthenosphere boundary (LAB) is defined here as the depth of the strongest negative velocity gradient at the base of the high velocity seismic lid.

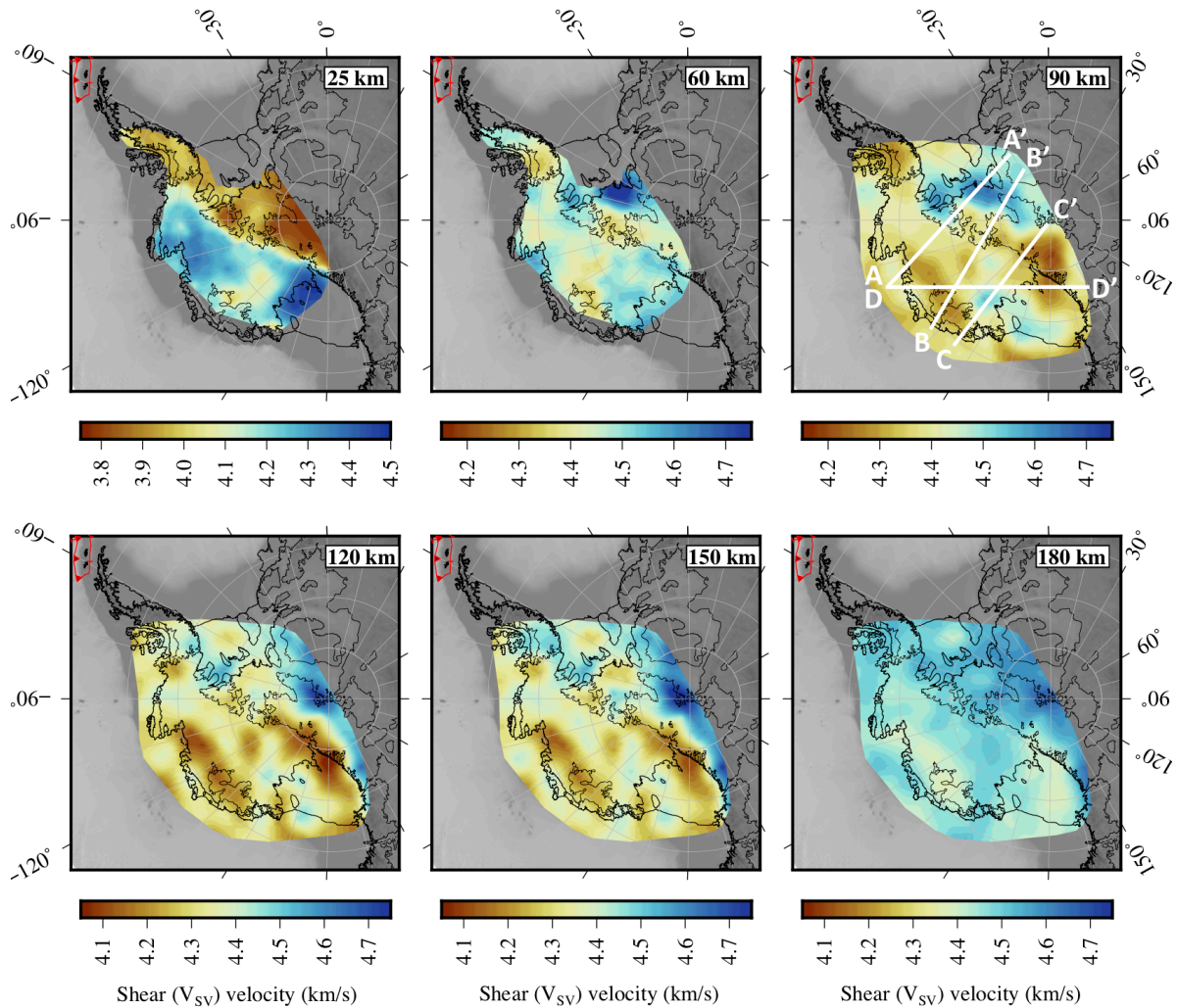


Figure 8: Shear wave velocity ( $V_{SV}$ ) maps at a selection of depths. We only interpret shallow ( $<60$  km depth) shear wave structure within the footprint of the ANT model. The ANT model domain is more confined than the 2PWT domain, reflected in the varying areal extent of the maps. Shifting scale bars are used to emphasise lateral velocity variations. The locations of the vertical  $V_{SV}$  cross-sections shown in Figure 9 are superimposed on the 90 km depth map.

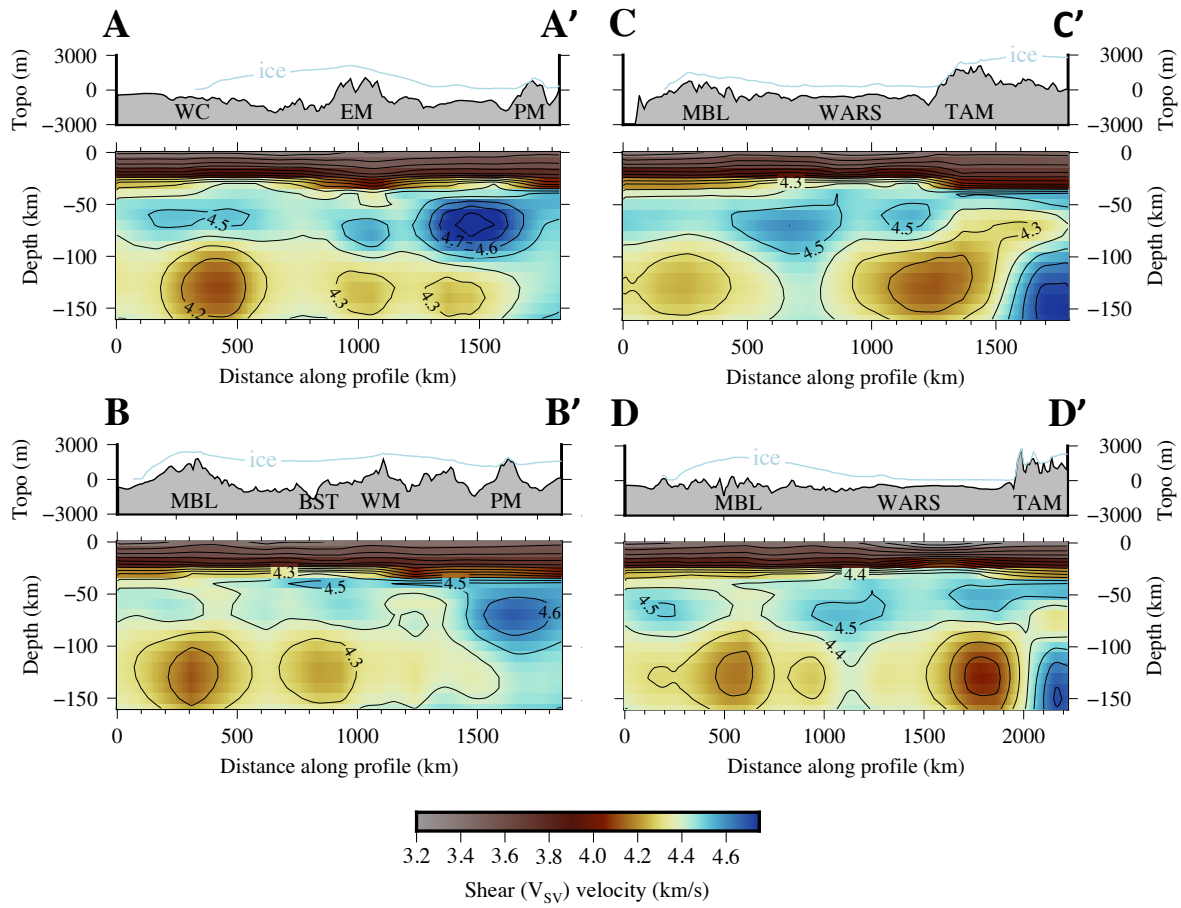


Figure 9: Vertical shear wave velocity ( $V_{SV}$ ) cross-sections along the four profiles located in Figure 8. The  $V_{SV}$  velocities are contoured at 0.1 km/s intervals. Corresponding BEDMAP2 ice and bedrock topography (Topo) profiles are shown in each case. BST, Bentley Subglacial Trench; EM, Ellsworth Mountains; MBL, Marie Byrd Land; PM, Pensacola Mountains; TAM, Transantarctic Mountains; WARS, West Antarctic Rift System; WC, Walgreen Coast; WM, Whitmore Mountains.

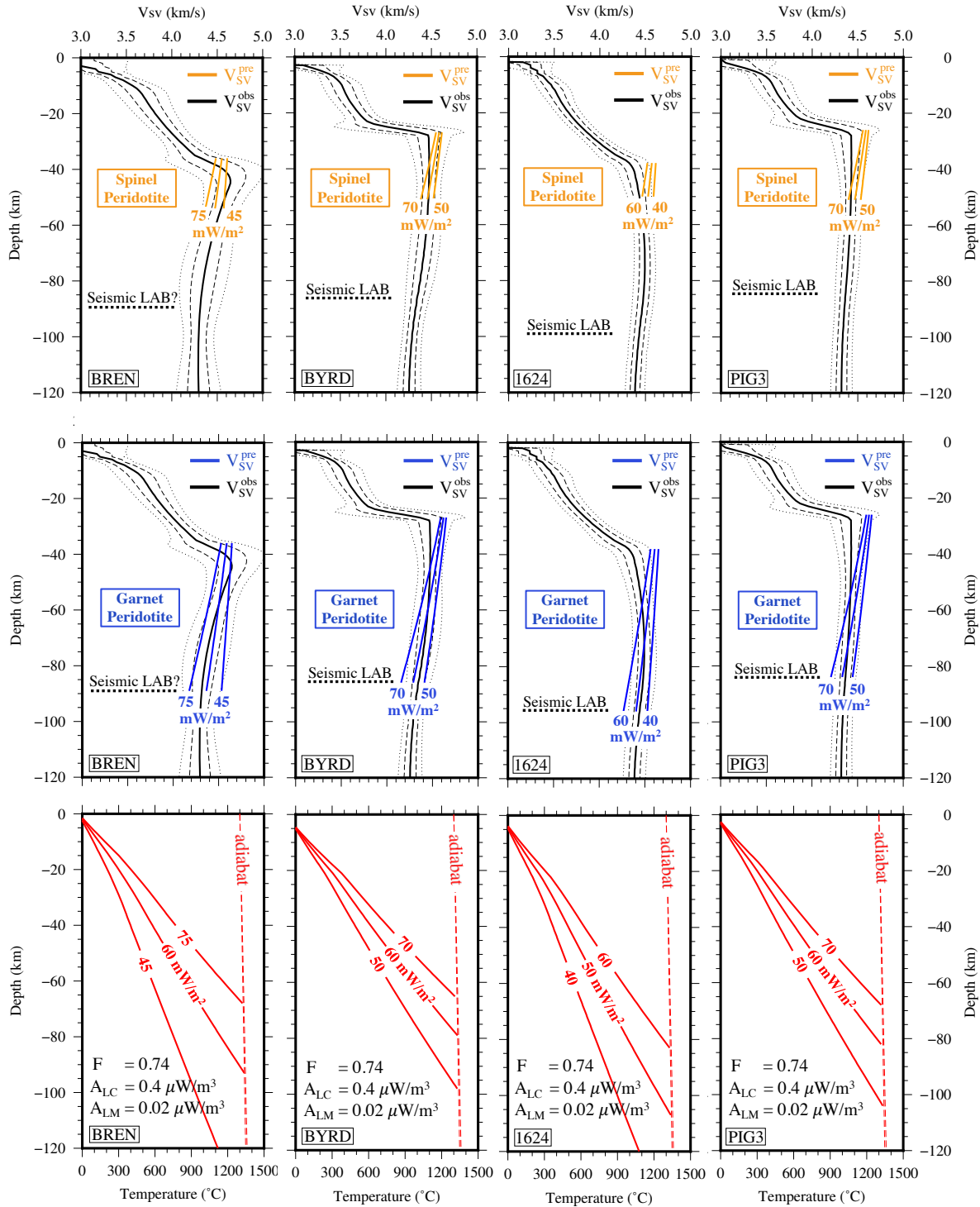


Figure 10: Observed and predicted  $V_{SV}$  velocities at seismic stations BREN (southern Antarctic Peninsula), BYRD (central WARS), PIG3 (adjacent to Pine Island Glacier in the Thurston Island block) and node 1624 (Ellsworth Mountains in the HEW block) for spinel peridotite (top) and garnet peridotite lithospheric mantle compositions (middle) corresponding to the steady-state conductive geotherms shown on the bottom. The continuous black  $V_{SV}$  profiles represent mean velocities, with dashed and dotted black lines representing one- and two-standard deviation bounds, respectively. Predicted velocity profiles and corresponding geotherms are labelled according to the surface heat flow.